Analytical scalings of the linear Richtmyer-Meshkov instability when a shock is reflected

F. Cobos Campos and J. G. Wouchuk*

E.T.S.I. Industriales, Instituto de Investigaciones Energéticas, and CYTEMA, Universidad de Castilla-La Mancha, 13071 Ciudad Real, Spain

(Received 29 July 2015; revised manuscript received 19 March 2016; published 18 May 2016)

When a planar shock hits a corrugated contact surface between two fluids, hydrodynamic perturbations are generated in both fluids that result in asymptotic normal and tangential velocity perturbations in the linear stage, the so called Richtmyer-Meshkov instability. In this work, explicit and exact analytical expansions of the asymptotic normal velocity (δv_i^∞) are presented for the general case in which a shock is reflected back. The expansions are derived from the conservation equations and take into account the whole perturbation history between the transmitted and reflected fronts. The important physical limits of weak and strong shocks and the high/low preshock density ratio at the contact surface are shown. An approximate expression for the normal velocity, valid even for high compression regimes, is given. A comparison with recent experimental data is done. The contact surface ripple growth is studied during the linear phase showing good agreement between theory and experiments done in a wide range of incident shock Mach numbers and preshock density ratios, for the cases in which the initial ripple amplitude is small enough. In particular, it is shown that in the linear asymptotic phase, the contact surface ripple (ψ_i) grows as $\psi_\infty + \delta v_i^\infty t$, where ψ_∞ is an asymptotic ordinate different from the postshock ripple amplitude at $t = 0+$. This work is a continuation of the calculations of F. Cobos Campos and J. G. Wouchuk, [Phys. Rev. E **90**, 053007 (2014)] for a single shock moving into one fluid.

DOI: 10.1103/PhysRevE.93.053111

I. INTRODUCTION

Since the middle of the last century much interest has been devoted to the study of the hydrodynamic perturbations that are created behind corrugated shock fronts [1–4]. We focus on the Richtmyer-Meshkov instability (RMI), which generally evolves after a planar shock hits a corrugated contact surface between two fluids. It has received considerable attention, either because of its importance in the success of the implosion of thermonuclear targets in inertial confinement fusion (ICF), in shock tube research and in the interaction with turbulent flows in general, or more recently, because of its inherent implications in the study of matter at high energy densities (HEDP) [5–37]. Anytime a planar shock front collides with a contact surface separating two fluids with different thermodynamic properties, a shock is transmitted and a shock or rarefaction wave is reflected back in the first fluid. We refer to Fig. 1, where an incident shock (not shown) has impinged with velocity D_i onto a contact surface located at $x = 0$, at $t = 0$. It came from the right and has compressed fluid b from ρ_{b0} to ρ_{b1}. The fluid velocity behind the incident shock is U_1. The material surface separates two ideal gases a and b that are initially at rest in the laboratory frame. The pressure in front of the incident shock is p_0, and p_1 is its value behind. We assume ideal gases with adiabatic exponents γ_a and γ_b. The sound speed of the uncompressed fluid b is $c_{b0} = \sqrt{\gamma_b p_0/\rho_{b0}}$. If we define the incident shock strength as $z_i = (p_1 - p_0)/p_0$, the incident shock Mach number M_i is given by [1]

$$M_i = \frac{D_i}{c_{b0}} = \sqrt{1 + \frac{\gamma_b + 1}{2\gamma_b} z_i}. \tag{1}$$

To the left of the contact surface, the other fluid has initial density ρ_{a0}. We define the initial density ratio between both gases as $R_0 = \rho_{a0}/\rho_{b0}$. At $t = 0+$, when the incident shock has completely disappeared, a transmitted shock travels to the left inside fluid a and a reflected shock or rarefaction moves to the right inside fluid b. In this work, we will only study the cases in which another shock is reflected back into fluid b. For a rarefaction to be driven back, the values of the initial parameters have to be chosen differently [9] and will not be considered in this work. For given values of γ_a, γ_b, and M_i, there is a minimum value of the preshock density ratio R_0^m, such that a shock is reflected only if $R_0 > R_0^m$. If the contact surface is corrugated with perturbation wavelength λ and initial ripple amplitude ψ_0, as indicated in Fig. 1, pressure and velocity perturbations are generated behind the rippled transmitted and reflected fronts. These perturbations consist of irrotational fluctuations in the form of evanescent sound waves and of vorticity or entropy perturbations which are frozen to the fluid elements for inviscid fluids [5,7,29,32–34]. In fact, due to the conservation of tangential velocity at the corrugated fronts, transverse velocity perturbations are generated inside the compressed fluids which account for vorticity generation in their bulks. This effect is stronger for stronger shocks and/or very compressible fluids [11,15,29]. For ideal gases, the shock ripples will decrease to zero when the shocks separate from the contact surface a distance greater than λ, which makes the pressure perturbations fade away in time. Hence, for a sufficiently long time after the incident shock refraction, the pressure perturbation field in the compressed fluids tends to zero. Therefore, the fluid acceleration vanishes in time and a quiescent velocity field emerges at both sides of the material surface. The velocity field attains its maximum value at the $x = 0$ surface and decays spatially at both sides. Very near the interface, the decay is mainly exponential, $\exp(-k|x|)$, where $k = 2\pi/\lambda$ and $|x|$ is the normal distance to the contact surface. However, far from the interface, the spatial decay of the velocity profile is controlled by the vorticity field generated by the rippled fronts [7,11] and, therefore, it shows an oscillatory decay with an envelope that vanishes with normal distance

*Gustavo.Wouchuk@uclm.es

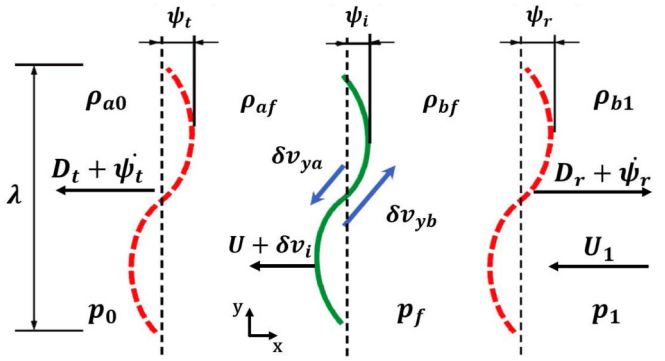

FIG. 1. A planar incident shock (not shown) has compressed fluid b from density ρ_{b0} to ρ_{b1} with pressure p_1. At $t = 0$, the incident shock arrives at the corrugated contact surface ($x = 0$). At $t > 0+$ a corrugated reflected shock moves to the right with velocity $D_r + \dot{\psi}_r(t)$. The transmitted shock moves into fluid a, to the left, with velocity $D_t + \dot{\psi}_t(t)$. Tangential velocities δv_{ya} and δv_{yb} evolve at both sides of the contact surface. At the same time, the material surface ripple grows with normal velocity $U + \delta v_i$.

as $(kx)^{-3/2}$ [11,15,38]. At the contact surface, the normal velocity reaches the value δv_i^∞ and the asymptotic tangential velocities at both sides are δv_{ya}^∞ and δv_{yb}^∞. The three velocities are not independent and are related in a specific way that is a function of the shock compression. In order to have bounded velocity perturbation fields far from the contact surface, we must require [11,15]

$$\begin{aligned} \left|\delta v_i^\infty\right| - \left|\delta v_{ya}^\infty\right| &= \mathcal{F}_a, \\ \left|\delta v_i^\infty\right| - \left|\delta v_{yb}^\infty\right| &= \mathcal{F}_b, \end{aligned} \tag{2}$$

where $\mathcal{F}_a$ and $\mathcal{F}_b$ are weighted averages of the vorticity generated behind the rippled shock waves in each fluid [11,15,17,39]. These two equations are the analogs of Eq. (42) of [39] and are the natural boundary conditions to be imposed at the contact surface when matching the asymptotic velocity fields of both fluids. The values of $\mathcal{F}_a$ and $\mathcal{F}_b$ are dependent on the whole perturbation evolution since $t = 0+$ and are a function of the incident shock strength as well as on the fluid compressibilities and initial density ratio [15,39]. Their exact values must be obtained by solving a set of coupled functional equations, which so far has resisted a closed analytical solution written with a finite number of terms, as explained in [15,39]. Despite the complexities in getting exact numerical values of $\mathcal{F}_a$ and $\mathcal{F}_b$, these quantities can be studied in different important physical limits by means of adequate Taylor expansions, or approximate expressions obtained by truncation of the iteration process involved in the solution of the corresponding equations. The aim of this work is to show accurate Taylor expansions in some important physical limits and an approximate expression of the asymptotic velocity at the contact surface approximately valid in a wide range of incident Mach numbers. Furthermore, a detailed study of the temporal evolution of the contact surface corrugation is presented over the time interval in which the perturbation evolves linearly. Recent experiments done with shock tubes spanning an interesting range of incident shock Mach numbers, preshock density ratios, and initial corrugation to wavelength ratios are analyzed with the theoretical tools provided in this work. The calculations shown here are an extension of the model published in Ref. [39]. Along this work we normalize the normal velocity, as suggested by [8], in units of $k\psi_0 D_i$ and define $u_i = \delta v_i^\infty/(k\psi_0 D_i)$. Each different physical limit will result in a corresponding expansion for the dimensionless normal velocity at the contact surface. We thus have

$$\begin{aligned} u_i &= a_1(M_i - 1) + a_2(M_i - 1)^2 + a_3(M_i - 1)^3 \\ &\quad + a_4(M_i - 1)^4 + O[(M_i - 1)^5], \quad M_i - 1 \ll 1, \\ u_i &= b_0 + \frac{b_1}{M_i^2} + O\left(\frac{1}{M_i^4}\right), \quad M_i \gg 1, \\ u_i &= c_0 + c_1\left(R_0 - R_0^m\right) + c_2\left(R_0 - R_0^m\right)^2 + c_3\left(R_0 - R_0^m\right)^3 \\ &\quad + c_4\left(R_0 - R_0^m\right)^4 + O\left[\left(R_0 - R_0^m\right)^5\right], \quad R - R_0^m \ll 1, \\ u_i &= d_0 + \frac{d_1}{R_0^{1/2}} + \frac{d_2}{R_0} + \frac{d_3}{R_0^{3/2}} + \frac{d_4}{R_0^2} \\ &\quad + O\left(\frac{1}{R_0^{5/2}}\right), \quad 1 \ll R_0 < \infty, \end{aligned} \tag{3}$$

where R_0^m is the minimum value of the preshock density ratio that warrants a shock reflected inside fluid b, for given values of γ_a, γ_b, and M_i. The coefficients appearing in the previous equations are calculated by expansion of the functional equations as Taylor series of the corresponding small parameter. The limits of very compressible fluid a and highly incompressible fluid b could also be studied on the same grounds, but we have found that the corresponding expansions would show a very small convergence radius. Therefore, a study of the growth rate in those limits would require a deeper analysis of the singularities of the background profiles in the complex plane, giving rise to quite involved calculations, and are left for future research.

This work is structured as follows: In Sec. II, the zero order profiles that relate the postshock quantities to M_i, R_0, γ_a, and γ_b are briefly discussed in the physical limits mentioned above, as they will be necessary later to get expansions such as those shown in Eq. (3). In Sec. III, the perturbation model derived in Ref. [15] is succinctly reviewed. The vorticity and asymptotic velocity fields are shown. The temporal evolution of the contact surface ripple $[\psi_i(t)]$ is analyzed and an asymptotic formula of the form $\psi_i(t) \cong \psi_\infty + \delta v_i^\infty t$ is obtained. An irrotational formula for δv_i^∞ and a more accurate expression for the normal velocity u_i are compared in Sec. IV. The Taylor expansions of the asymptotic velocities in different important physical limits are shown in Sec. V. In particular, differences between the estimates of u_i given here and older approximations provided by impulsive formulations are analyzed when discussing the weak shock limit. A comparison with recent simulations and experiments is given in Sec. VI, where the observed values of ψ^∞ and δv_i^∞ are compared with the predictions of the model presented in this work. A summary is given in Sec. VII.

II. ZERO ORDER PROFILES

In order to develop the analytical expansions shown above for the late time asymptotic velocities, we need to briefly

discuss the postshock values of the physical quantities in both compressed fluids. We start with the quantities behind the incident shock. The incident density ratio ρ_{b1}/ρ_{b0}, the incident sound speed ratio c_{b1}/c_{b0}, and the incident dimensionless bulk velocity U_1/c_{b0} are, respectively,

$$\frac{\rho_{b1}}{\rho_{b0}} = \frac{2\gamma_b + (\gamma_b+1)z_i}{2\gamma_b + (\gamma_b-1)z_i} = \frac{(\gamma_b+1)M_i^2}{(\gamma_b-1)M_i^2+2},$$

$$\frac{c_{b1}}{c_{b0}} = \sqrt{\frac{1+z_i}{R_i}} = \frac{\sqrt{\left(2\gamma_b M_i^2 - \gamma_b + 1\right)\left[(\gamma_b-1)M_i^2+1\right]}}{(\gamma_b+1)M_i},$$

$$\frac{U_1}{c_{b0}} = \frac{z_i}{\gamma_b\sqrt{1+\frac{\gamma_b+1}{2\gamma_b}z_i}} = \frac{2}{\gamma_b+1}\left(M_i - \frac{1}{M_i}\right). \tag{4}$$

As shown in Fig. 1, the reflected shock travels with velocity D_r and the transmitted front with D_t in the laboratory frame. The fluid velocity in the space between both refracted fronts is U. The final density of fluid b is ρ_{bf} and its pressure is p_f. The sound speed behind the reflected front is $c_{bf} = \sqrt{\gamma_b p_f/\rho_{bf}}$. The pressure between the reflected front and the transmitted shock is equal to p_f. The density of fluid a behind the transmitted front is ρ_{af}. The sound velocity of the uncompressed fluid a is $c_{a0} = \sqrt{\gamma_a p_0/\rho_{a0}}$ and its compressed value is $c_{af} = \sqrt{\gamma_a p_f/\rho_{af}}$. Following [40], we define the relative pressure jumps at the reflected and transmitted shocks:

$$z_r = \frac{p_f - p_1}{p_1}, \quad z_t = \frac{p_f - p_0}{p_0}. \tag{5}$$

Behind the reflected and the transmitted shock waves we have, respectively, the upstream (M_r, M_t) and downstream (β_r, β_t) Mach numbers:

$$M_r = \sqrt{1+\frac{\gamma_b+1}{2\gamma_b}z_r}, \quad M_t = \sqrt{1+\frac{\gamma_a+1}{2\gamma_a}z_t},$$

$$\beta_r = \sqrt{\frac{2\gamma_b+(\gamma_b-1)z_r}{2\gamma_b(1+z_r)}} = \sqrt{\frac{(\gamma_b-1)M_r^2+2}{2\gamma_b M_r^2 - \gamma_b + 1}},$$

$$\beta_t = \sqrt{\frac{2\gamma_a+(\gamma_a-1)z_t}{2\gamma_a(1+z_t)}} = \sqrt{\frac{(\gamma_a-1)M_t^2+2}{2\gamma_a M_t^2 - \gamma_a + 1}}. \tag{6}$$

We also have

$$\frac{\rho_{bf}}{\rho_{b1}} = \frac{2\gamma_b+(\gamma_b+1)z_r}{2\gamma_b+(\gamma_b-1)z_r} = \frac{(\gamma_b+1)M_r^2}{(\gamma_b-1)M_r^2+2},$$

$$\frac{\rho_{af}}{\rho_{a0}} = \frac{2\gamma_a+(\gamma_a+1)z_t}{2\gamma_a+(\gamma_a-1)z_t} = \frac{(\gamma_a+1)M_t^2}{(\gamma_a-1)M_t^2+2},$$

$$\frac{c_{bf}}{c_{b1}} = \sqrt{\frac{1+z_r}{R_r}} = \frac{\sqrt{\left(2\gamma_b M_r^2 - \gamma_b + 1\right)\left[(\gamma_b-1)M_r^2+1\right]}}{(\gamma_b+1)M_r},$$

$$\frac{c_{af}}{c_{a0}} = \sqrt{\frac{1+z_t}{R_t}} = \frac{\sqrt{\left(2\gamma_a M_t^2 - \gamma_a + 1\right)\left[(\gamma_a-1)M_t^2+1\right]}}{(\gamma_a+1)M_t},$$

$$\frac{U_1 - U}{c_{b1}} = \frac{z_r}{\gamma_b\sqrt{1+\frac{\gamma_b+1}{2\gamma_b}z_r}} = \frac{2}{\gamma_b+1}\left(M_r - \frac{1}{M_r}\right),$$

$$\frac{U}{c_{a0}} = \frac{z_t}{\gamma_a\sqrt{1+\frac{\gamma_a+1}{2\gamma_a}z_t}} = \frac{2}{\gamma_a+1}\left(M_t - \frac{1}{M_t}\right). \tag{7}$$

We define the postshock density ratio and the postshock sound speed ratio at the contact surface as

$$R = \frac{\rho_{af}}{\rho_{bf}} = \frac{\rho_{af}}{\rho_{a0}}\frac{\rho_{b1}}{\rho_{bf}}\frac{\rho_{b0}}{\rho_{b1}}R_0,$$

$$N = \frac{c_{af}}{c_{bf}} = \frac{c_{af}}{c_{a0}}\frac{c_{b1}}{c_{bf}}\frac{c_{b0}}{c_{b1}}\sqrt{\frac{\gamma_a}{\gamma_b R_0}}. \tag{8}$$

The reflected and transmitted shock strength parameters z_r and z_t are related to the incident shock strength (z_i), preshock density ratio (R_0), and fluid compressibilities (γ_a, γ_b) through continuity of pressure and normal velocity at the contact surface. We have

$$z_t = z_i + (1+z_i)z_r, \tag{9}$$

$$\frac{z_i}{\sqrt{2\gamma_b+(\gamma_b+1)z_i}} - \frac{c_{b1}}{c_{b0}}\frac{z_r}{\sqrt{2\gamma_b+(\gamma_b+1)z_r}} = \frac{1}{\sqrt{R_0}}\frac{z_t}{\sqrt{2\gamma_a+(\gamma_a+1)z_t}}. \tag{10}$$

Recently, the solutions of the above equations have been successfully compared with numerical simulations either in the weak or strong shock limits and in the high/low preshock density contrast at the contact surface in [24–27].

As discussed in Ref. [9], we can go continuously from the case in which a shock is reflected to the case in which a rarefaction wave is driven inside fluid b, just by changing the ratio of initial densities at the material surface, for given values of γ_a, γ_b, and M_i. In fact, if $R_0 \to \infty$, the situation resembles that of a rigid wall and a shock is always reflected back. This case has been studied in [39]. If we start decreasing the initial density ratio, a shock is still being reflected until, for some value of $R_0 = R_0^m$, there is no reflected shock. In this case, it is $z_r = 0$, a situation that is called *total transmission*. The mathematical hypersurface (in the space $\{R_0, \gamma_a, \gamma_b, z_i\}$) that describes total transmission can be determined by simply asking $z_r = 0$ in Eqs. (9) and (10). For values $R_0 < R_0^m$ a rarefaction is reflected back and a shock will be driven back if $R_0 > R_0^m$. It is easy to see that

$$R_0^m = \frac{\gamma_b(\gamma_b+1)M_i^2}{\gamma_a - \gamma_b + \gamma_b(\gamma_a+1)M_i^2}. \tag{11}$$

From the above equation we see that if $\gamma_a < \gamma_b$, for a given value of the incident Mach number (M_i), a shock will be reflected only from a light to heavy interaction ($\rho_{b0} < \rho_{a0}$), in accordance with [8,9]. On the contrary, if $\gamma_a > \gamma_b$, a shock is also reflected for a light to heavy interaction ($\rho_{a0} < \rho_{b0}$) and sometimes for a heavy to light interaction. If $\gamma_a = \gamma_b$, it is $R_0^m = 1$. The value of R_0^m will be useful later when studying the instability growth at a low preshock density ratio.

The solution of Eqs. (9) and (10) does not seem to be easily expressed in closed analytical form for arbitrary values of the preshock parameters, and it is much easier to solve them numerically in order to compute the postshock quantities in both fluids. Up to date, no analytical solution to the above equations has been reported in the literature. For very weak

shocks, the postshock quantities of the compressed fluids can always be expanded in powers of $M_i - 1$. From Eqs. (9) and (10), we can write for M_r, in the limit $z_i \ll 1$,

$$M_r = 1 + m_r^{w1}(M_i - 1) + O[(M_i - 1)^2], \tag{12}$$

and these coefficients are used in the intermediate calculations necessary to obtain the coefficients a_1, a_2, a_3, a_4 of Eq. (3). As they are rather involved functions of their arguments, they are not explicitly shown here. See the Supplemental Material [41] for retrieving the coefficients of the expansion. Similarly, the other zero order quantities such as M_t can be expanded in powers of $M_i - 1$ and the corresponding coefficients will be functions of those in Eq. (12).

An expansion in powers of $1/M_i$ can be sought for very strong shocks. In fact, it can be written as

$$M_r = m_r^{s\infty} + \frac{m_r^{s1}}{M_i^2} + O\left(\frac{1}{M_i^4}\right). \tag{13}$$

See the Supplemental Material [41] for the values of $m_r^{s\infty}$ and m_r^{s1}, which are necessary to calculate the coefficients b_0 and b_1 of Eq. (3). In particular $m_r^{s\infty}$ is the root of a fourth degree polynomial which can always be expressed in closed analytical form. In the limit $R_0 - R_0^m \ll 1$, an expansion of the form is tried:

$$M_r = 1 + m_r^{m1}\left(R_0 - R_0^m\right) + O\left[\left(R_0 - R_0^m\right)^2\right], \tag{14}$$

the coefficients of which are shown in the corresponding Supplemental Material [41]. Analogously, in the limit $R_0 \gg 1$, the expansion

$$M_r = m_r^{ld\infty} + \frac{m_r^{ld1}}{\sqrt{R_0}} + O\left[\frac{1}{R_0}\right] \tag{15}$$

is sought. Equations (12), (13), (14), and (15) will be used when studying the asymptotic velocities in different limits (weak or strong shocks, high or low preshock density ratio).

III. LINEARIZED EQUATIONS

In this section we show the linearized equations that describe the perturbed shock dynamics and the achievement of the asymptotic velocity profiles in both fluids within the limits of validity of a linear theory. A brief account of known results, already shown in previous works, is necessary here in order to follow the discussion of the following sections, while keeping the repeated material to a minimum. As usual, our contact surface has a corrugation with wavelength λ and amplitude $\psi_0 \ll \lambda$ and we study the perturbation problem in a system comoving with the compressed fluids. As a result of the incident shock-contact surface interaction, a tangential velocity shear is generated at $t = 0+$, when the incident shock has completely disappeared and the reflected and transmitted fronts are generated. As widely discussed since the first work of Richtmyer [5–9,11,13–17,20–24,29,32–35], the conservation of tangential momentum across the corrugated fronts is responsible in generating a tangential velocity perturbation downstream. The values of the initial tangential velocities are given by [5,15]

$$\delta v_{ya}^0 = -Uk\psi_{t0}, \quad \delta v_{yb}^0 = (U_1 - U)k\psi_{r0}, \tag{16}$$

where the initial corrugations of the transmitted and reflected shocks are [10,11,15]

$$\psi_{t0} = \left(1 - \frac{D_t}{D_i}\right)\psi_0, \quad \psi_{r0} = \left(1 + \frac{D_r}{D_i}\right)\psi_0. \tag{17}$$

Due to the lateral mass flows induced by the above tangential velocities, pressure gradients are created in both fluids once the shocks start to separate from the surface. As a result, sound waves are generated in the space between the rippled shock fronts and the material surface. The shock ripples oscillate in time and besides acoustic fluctuations, vorticity and entropy perturbations will be also generated. For nondissipative fluids, vorticity and entropy will remain frozen to the fluid elements. As the shocks separate away their ripple amplitudes will decay in an oscillatory fashion and the pressure fluctuations created at the shock wave fronts will also decay in time. Therefore, after some characteristic time [on the order of the maximum between $\lambda/(D_r + U_1 - U)$ and $\lambda/(D_t - U)$] the wave fronts regain planarity and the pressure perturbation fields vanish. Then, a steady state velocity field slowly emerges in both fluids. The maximum value of the perturbation velocities is achieved at the material surface itself. As highlighted in Eq. (2), these velocities are interrelated and are dependent on the whole perturbation history ($0+ < t < \infty$) through the quantities $\mathcal{F}_a$ and $\mathcal{F}_b$, which are a weighted average of the shocks' pressure perturbations. This means that any consistent analytic model that tries to calculate the contact surface velocities has to consider the dynamical evolution of the pressure fluctuation fields in both compressed fluids, at least for shocks of moderate to high strength [39]. In order to solve the dynamical equations in both fluids, it is better to use nondimensional quantities which we define below. We use the incident shock speed D_i to normalize the velocities. For fluid m, where $m = a$ or b, we write pressure, density, and normal and tangential velocity perturbations:

$$\begin{aligned}
\frac{\delta p_m}{\rho_{mf} D_i c_{mf}} &= k\psi_0 \tilde{p}_m(x,t)\cos ky, \\
\frac{\delta \rho_m}{\rho_{mf}} &= k\psi_0 \tilde{\rho}_m(x,t)\cos ky, \\
\frac{\delta v_{xm}}{D_i} &= k\psi_0 \tilde{v}_{xm}(x,t)\cos ky, \\
\frac{\delta v_{ym}}{D_i} &= k\psi_0 \tilde{v}_{ym}(x,t)\sin ky.
\end{aligned} \tag{18}$$

The dimensionless initial tangential velocities are written as $\tilde{v}_{ya}^0$ and $\tilde{v}_{yb}^0$.

A. Solution of the fluid equations for the pressure perturbations downstream from each rippled wave front

The fluid equations must be solved in both compressed fluids since $t = 0+$. For the sake of simplicity, the index m that identifies each fluid is omitted in this subsection. We define the dimensionless variables $\tilde{x} = kx$ and $\tau = kc_{mf}t$. The equations of motion in each fluid lead us to the homogeneous wave equation for the pressure perturbations:

$$\frac{\partial^2 \tilde{p}}{\partial \tau^2} = \frac{\partial^2 \tilde{p}}{\partial \tilde{x}^2} - \tilde{p}. \tag{19}$$

As usual in previous works, we make the coordinate transformation suggested by Zaidel [2,3], and extensively used in [15,29,32,33,39]. We change from the Cartesian coordinates x,t to the new variables r,χ by means of the transformation

$$\tilde{x} = r\sinh\chi, \quad \tau = r\cosh\chi. \tag{20}$$

A surface defined by $\chi =$ constant represents a planar front moving between the contact surface and the corresponding shock front along the trajectory: $\tilde{x} = \tau\tanh\chi$. The shock fronts have "constant" values of their χ coordinates. Due to this fact, the coordinate r at each shock front is proportional to time. The fluid equations can be combined into a coupled set of equations in the variables r,χ:

$$r\frac{\partial^2\tilde{p}}{\partial r^2} + \frac{\partial\tilde{p}}{\partial r} + r\tilde{p} = \frac{\partial\tilde{h}}{\partial\chi},$$
$$\tilde{h} = \frac{1}{r}\frac{\partial\tilde{p}}{\partial\chi}. \tag{21}$$

It is clear that Eqs. (21) are equivalent to (19). There are two ways to present the solution of Eqs. (21): by separation of variables as in [10] or by means of Laplace transforms [10,15,21,29]. Both approaches are useful for us in this work and are briefly reviewed.

1. *Solution of the pressure wave equation by separation of variables*

The system of coordinates χ,r allows us to use the method of separation of variables, because each shock front has a constant value of the χ coordinate. We can easily arrive at a solution for $\tilde{p}$ and $\tilde{h}$ of the form [10]

$$\tilde{p}(\chi,r) = \sum_{j=0}^{\infty} D_{2j+1}(\chi)J_{2j+1}(r),$$
$$\tilde{h}(\chi,r) = \sum_{j=0}^{\infty} E_{2j+1}(\chi)\frac{(2j+1)J_{2j+1}(r)}{r}, \tag{22}$$

where

$$D_{2j+1}(\chi) = \pi_{2j+1}\cosh(2j+1)\chi + \omega_{2j+1}\sinh(2j+1)\chi,$$
$$E_{2j+1}(\chi) = \omega_{2n+1}\cosh(2j+1)\chi + \pi_{2j+1}\sinh(2j+1)\chi. \tag{23}$$

The set of coefficients π_{2j+1} and ω_{2j+1} have to be determined with the initial and boundary conditions at the shocks and contact surface. There is a set of such coefficients for each fluid, and hence, they compose a set of four denumerable arrays of infinite coefficients. They can be calculated with the aid of the mathematical formalism outlined in [10]. The functions J_{2j+1} in Eqs. (22) are the ordinary Bessel functions. With the solution given in Eqs. (22) we have complete information of the temporal evolution of the pressure perturbations and hence of all the perturbation quantities. However, in order to get the important quantities $\mathcal{F}_a$ and $\mathcal{F}_b$ for any shock strength or other important physical limits, it will be convenient to solve the pressure wave equation by means of the Laplace transform. This is because the quantities $\mathcal{F}_a$ and $\mathcal{F}_b$ are actually proportional to particular values of the Laplace transforms (in time) of the pressure fluctuations at each shock. The quantities $\mathcal{F}_m$ could be, of course, calculated with Eqs. (22), but convergence of the series is very slow for moderate to strong shocks. With this scope in mind, we review next the procedure involving Laplace transformations.

2. *Solution of the pressure wave equation by Laplace transforms*

For any quantity of interest $\phi(\chi,r)$ we define its Laplace transform integrating the variable r in the form [2,3,15,21,29]

$$\Phi(\chi,s) = \int_0^{\infty}\phi(\chi,r)\exp(-sr)\,dr. \tag{24}$$

We define $s = \sinh q$, and transform Eqs. (21) in the domain of the variables χ,q. It can be seen after some algebraic manipulations that the Laplace transforms of the pressure perturbations $\tilde{p}$ and $\tilde{h}$ [defined in Eq. (22)] can be expressed as

$$\tilde{P}(\chi,q) = \frac{F_1(q-\chi) + F_2(q+\chi)}{\cosh q},$$
$$\tilde{H}(\chi,q) = F_1(q-\chi) - F_2(q+\chi), \tag{25}$$

for some adequate functions F_1 and F_2, which are determined by considering the linearized Rankine-Hugoniot equations at each shock front together with the continuity of pressure and normal velocity at the contact surface plus initial conditions. The procedure to obtain approximate or more accurate expressions of the pressure amplitudes F_1 and F_2 is reviewed in Appendix A. From them, we obtain $\tilde{P}_{a,b}$ in each fluid and, formally speaking, we get the pressure perturbations in the space-time domain of the variables $\tilde{x},\tau_m$ with a standard inverse Laplace transformation ($m = a,b$). Formally speaking, the pressure perturbations in real-time domain, at any position (χ_m,r_m), would be expressed by an integral in the complex plane:

$$\tilde{p}(\chi_m,r_m) = \frac{1}{2\pi i}\int_{c-i\infty}^{c+i\infty}\tilde{P}(\chi_m,s_m)\exp(s_m r_m)\,ds_m, \tag{26}$$

where the real number c is chosen to the right of all the singularities of the integrand and i is the imaginary unit ($i^2 = -1$). For the problems involving RM-like flows, the above integral will reduce to a sequence of real integrals along the branch cuts, usually located on the imaginary axis, generated because of the multivaluedness of the function $\sqrt{s_m^2+1}$ in each fluid, appearing in the auxiliary functions ϕ defined in Appendix A. This technique has been successfully employed in [17,29,32–34] to study the interaction of isolated shock fronts with isotropic turbulent flows. For the case of two fluids in this work, the results obtained from Eq. (26) agree with the alternative approach given by the series of Bessel functions [Eqs. (22) and (23)]. Our purpose here is to use the information provided by Eqs. (A5) in order to calculate the quantities $\mathcal{F}_a$ and $\mathcal{F}_b$ with approximate expressions and also to obtain adequate expansions in different physical limits as well as to follow the dynamical evolution of the linear perturbations in time, when necessary. The solution of the pressure functions F_{m1} and F_{m2} would require iterating a finite number of times, as explained in Appendix A. The exact number of iterations used ($n = 0,1,2,3,\ldots$) would depend on the level of compression.

B. Velocity perturbations: Asymptotic velocity field

When the shocks have separated from the contact surface, a steady velocity field remains and we define the velocity vector $\vec{v} = (\tilde{v}_x, \tilde{v}_y)$. Vorticity is only generated at the shock fronts. In the system of reference comoving with the compressed fluids, the vorticity is frozen to the fluid particles, and therefore it is a steady state vector field that does not change in time, in the absence of viscosity. Thus, the velocity field can be decomposed as the sum of two parts: one that corresponds to the steady state vorticity distribution ($\vec{\tilde{v}}_{rot}$) and the other corresponding to the irrotational motion induced by the pressure sound waves ($\vec{\tilde{v}}_{ac}$) [29,32,33]:

$$\vec{\tilde{v}}(x,y,t) = \vec{\tilde{v}}_{rot}(x,y) + \vec{\tilde{v}}_{ac}(x,y,t). \tag{27}$$

When the shocks are far enough from the contact surface, the contribution from the pressure field vanishes and, hence, the irrotational component of the velocity decreases to zero, and only the rotational component remains as a steady velocity distribution. The rotational part of the velocity distribution is written here in the following way:

$$\vec{\tilde{v}}_{rot} = (u(x)\cos ky, v(x)\sin ky). \tag{28}$$

The differential equations satisfied by the functions $u(x)$ and $v(x)$ are shown in Appendix B. The asymptotic velocities at both sides of the material surface (at $x = 0$) are not independent, but are related to each other through the compressible evolution in both fluids [see Eq. (2)]. The difference between the absolute values of the normal and tangential velocities, at each side, is a precise functional of the pressure perturbations behind the corresponding rippled front. In fact, after some algebra, we write, according to Eq. (B9),

$$\begin{aligned} |u_i| - |v_{ia}| &= -\Omega_a \sinh\chi_t \tilde{P}(q_a = -\chi_t) = F_a, \\ |u_i| - |v_{ib}| &= \Omega_b \sinh\chi_r \tilde{P}(q_b = \chi_r) = -F_b, \end{aligned} \tag{29}$$

where F_m is the dimensionless form of $\mathcal{F}_m$ [Eqs. (2)]. The quantities Ω_a and Ω_b are given in Eqs. (B4) of Appendix B. The relationships outlined in Eqs. (29) are the same as Eq. (42) of [39] for a single fluid. In the problem considered here, we still need a third equation, which is obtained integrating the y component of the linearized momentum equation at the contact surface in the interval $0+ < t < \infty$, as shown in [10,11,15]. We obtain

$$R\left(v_{ia} - \tilde{v}^0_{ya}\right) = v_{ib} - \tilde{v}^0_{yb}. \tag{30}$$

Combining the last three equations we get

$$\begin{aligned} u_i &= \frac{\tilde{v}^0_{yb} - R\tilde{v}^0_{ya}}{R+1} + \frac{RF_a - F_b}{R+1}, \\ v_{ia} &= -\frac{\tilde{v}^0_{yb} - R\tilde{v}^0_{ya}}{R+1} + \frac{F_a + F_b}{R+1}, \\ v_{ib} &= \frac{\tilde{v}^0_{yb} - R\tilde{v}^0_{ya}}{R+1} + \frac{R(F_a + F_b)}{R+1}. \end{aligned} \tag{31}$$

The asymptotic velocities at the contact surface are the sum of two terms: the first one is dependent on the initial transverse velocities generated at $t = 0+$ and the second term takes into account the whole perturbation history and can be seen as a functional of both vorticity fields. In fact, F_a and F_b are a weighted measure of the concentration of vorticity spread in the bulk of both fluids.

C. Calculation of F_a and F_b

As was shown in [39], a relatively simple and quite accurate formula for the asymptotic tangential or normal velocities in a single fluid can be obtained from the functional equation satisfied by the Laplace transform of the shock pressure perturbations. The same is true in the case of two fluids as briefly discussed in [15]. In any case, the bulk vorticity parameters (F_a and F_b) are always required. After some algebra with the boundary conditions at the interface and using the expressions of the Laplace transforms of the pressure perturbations [Eq. (25)] we can write the following exact expressions [15], which will be needed for future discussion:

$$\begin{aligned} F_a &= \left[1 + \frac{M_t^2}{M_t^2 - 1}\frac{4(D_t - U)}{U_i}\right]^{-1}\left[\tilde{v}^0_{ya} - 2F_{a1}(-2\chi_t)\right], \\ F_b &= \left[1 + \frac{M_r^2}{M_r^2 - 1}\frac{4(D_r + U_i)}{U_1 - U_i}\right]^{-1}\left[\tilde{v}^0_{yb} - 2F_{b2}(2\chi_r)\right]. \end{aligned} \tag{32}$$

The main difficulty to calculate F_a and F_b lies in getting accurate enough estimates of the pressure functions $F_{a1}(-2\chi_t)$ and $F_{b2}(2\chi_r)$. As shown in previous works and briefly sketched in Appendix A, the functions F_{m1} and F_{m2} can be calculated by iteration over a system of coupled functional equations. We thus get a hierarchy of improved estimations: $F^{[n]}_{m1}$ and $F^{[n]}_{m2}$, with $n \geqslant 0$. The number of steps n used would be dependent on the range of the preshock parameters we explore. It is chosen to ensure at least three digits in the final results. For most of the cases found in actual experiments or in simulations, the initial functions are enough (that is, $n = 0$). Of course, with only $F^{[0]}_{a1}$ and $F^{[0]}_{b2}$, the accuracy will decrease when we go to stronger shocks or higher density ratios, or deal with situations where one or both fluids are highly compressible. These cases will be discussed in the next section. Without iteration, a first approximate estimate of the vorticity averages F_a and F_b is

$$\begin{aligned} F^{[0]}_a &= \left[1 + \frac{M_t^2}{M_t^2 - 1}\frac{4(D_t - U)}{U_i}\right]^{-1}\left[\tilde{v}^0_{ya} - 2F^{[0]}_{a1}(-2\chi_t)\right], \\ F^{[0]}_b &= \left[1 + \frac{M_r^2}{M_r^2 - 1}\frac{4(D_r + U_i)}{U_1 - U_i}\right]^{-1}\left[\tilde{v}^0_{yb} - 2F^{[0]}_{b2}(2\chi_r)\right], \end{aligned} \tag{33}$$

where the functions $F^{[0]}_{a1}$ and $F^{[0]}_{b2}$ are shown in Appendix A.

When computing, for example, $F^{[0]}_{a1}(-2\chi_t)$ with the aid of the second of Eq. (A7), care must be taken of using the correct value of q_b for that equation: $q_b = \sinh^{-1}(-N\sinh 2\chi_t)$. On the other hand, to compute $F^{[0]}_{b2}(2\chi_r)$ with the first of Eq. (A7), we must be careful in order to consider the correct value of q_a inside that equation: $q_a = \sinh^{-1}[(\sinh 2\chi_r)/N]$. Higher orders of iteration can be easily obtained. We use the functions obtained in Eqs. (A7) as seed values and substitute them on the right hand sides of Eqs. (33). In this way, a new set of functions called $F^{[1]}_{a1}$, $F^{[1]}_{b2}$ is obtained. Using them as seed functions, a new iteration order $F^{[2]}_{a1}$, $F^{[2]}_{b2}$ can be obtained, and

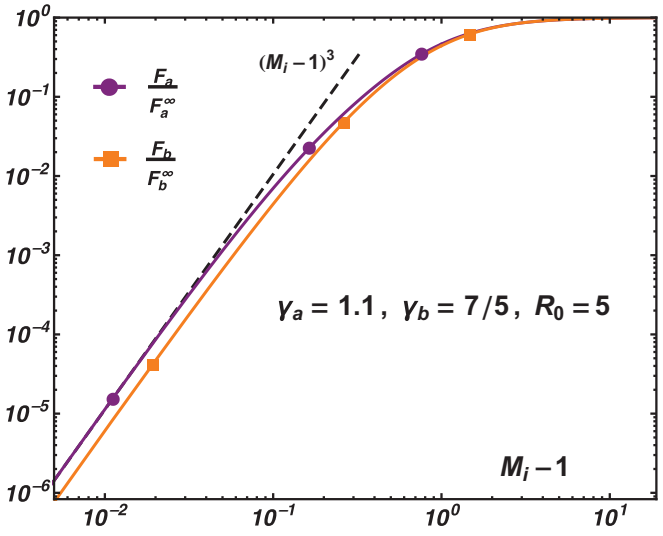

FIG. 2. Dependence of the bulk vorticity parameters F_a and F_b on the incident shock Mach number (M_i) for the given pair of gases. The vorticity parameters are normalized with their values at high compression ($F_a^\infty = -0.1174$, $F_b^\infty = 0.0157$). The weak shock scaling is indicated with a dashed line.

so on. This is the procedure to get improved values $F_a^{[n]}$ and $F_b^{[n]}$ of the vorticity parameters. We have iterated almost five times to get three or more significant digits in the asymptotic velocities (the exact number strongly depends on the range of parameters under study) and those results are used here as reference values for comparison.

In Fig. 2 we show the quantities F_a and F_b normalized with their values at high compression, achieved for very strong shocks. The calculations have been done with 5 iterations and the gases are $\gamma_a = 1.1$ and $\gamma_b = 7/5$. The preshock density ratio is $R_0 = 5$. For very strong shocks, the bulk parameters saturate and their values are $F_a^\infty = -0.1174$ and $F_b^\infty = 0.0157$. It can be shown, using the formulas developed before, that $F_a, F_b \sim (M_i - 1)^3$, in the weak shock limit. This scaling is easily recognized in the log-log plot of Fig. 2. Usually, it is $F_a \gg F_b$. Besides, F_a and F_b have, in general, opposite sign. This is due to the mechanism of tangential velocity generation behind each rippled front which makes the initial tangential velocities to be of opposite sign, except at freeze-out [17,42–44]. The dependence of $F_{a,b}$ as functions of the preshock parameters is important, because it indicates the quantitative difference between the normal and tangential velocity at both sides of the interface ripple, in each fluid [see Eq. (29)], telling us how much the velocity field departs from a potential solution.

In Fig. 3 we show the velocity and vorticity space profiles for a particular case: the incident shock Mach number is $M_i = 5$ and the fluids have $\gamma_a = 1.1$, $\gamma_b = 1.182$. The preshock contact surface density ratio is $R_0 = 5$. These values have been chosen for the sake of simplicity in manipulating the series of Bessel functions involved in the calculations. As $c_{af} = c_{bf}$ for this case, convergence is quite fast. The normal and tangential velocities as well as the vorticity profile are solutions of the equations shown in Appendix B. To obtain the vorticity density map, we need the temporal evolution of the shocks' pressure perturbations. Two approaches have been used for this purpose. On one side, the coefficients of the series of Bessel functions shown in Eqs. (22) and (23) have been calculated following [11]. On the other hand, an inverse Laplace transformation, using Eqs. (25) and (26) and the results of Appendix A were used. Both approaches give the same results. In Fig. 3(a) we show the normal velocity profiles at both sides of the contact surface. It is seen that on the side of the reflected shock, the normal velocity is approximately well described by a decaying exponential near the material surface and later it shows a gentle phase inversion, due to the presence of vorticity in that fluid. On the side of fluid a, the normal velocity profile shows more oscillations in space, as vorticity is usually stronger. The exponential function is, in general, not a good approximation for the velocity perturbations on the side of the transmitted shock. In Fig. 3(b) we show the profile of the asymptotic tangential velocity. For the conditions of Fig. 3, an exponential approximation is better on side b than on fluid a. The exponential approximation on side b, where the reflected shock traveled, is only good for $0 \leqslant |x|/\lambda \lesssim 0.3$ or $0 \leqslant k\,|x| \lesssim 2$. If we made $\delta v_x \sim u_i \exp(-kx)$ inside fluid b, incompressibility would require $\delta v_y \sim u_i \exp(-kx)$. If we made a zoom inside the denser fluid, near the material surface, we would see that an exponential approximation to the normal velocity is only valid within an extremely short distance from the contact surface: $0 \leqslant |x|/\lambda \lesssim 0.01$, or equivalently, $0 \leqslant k|x| \lesssim 0.06$. But using an exponential function to describe the spatial variation of δv_x inside a would give a wrong estimate of the tangential velocity in that fluid. In fact, if inside fluid a we made $\delta v_x \sim u_i \exp(kx)$, we must require, because of mass conservation, $\delta v_y \sim -u_i \exp(kx)$, which evidently does not describe the lateral mass flow associated with δv_y at the left of the contact surface. A potential flow model is a poor description for the velocity inside the denser fluid, in the conditions of Fig. 3. As will be discussed in Fig. 9, the normal and tangential velocities are very different at the contact surface, for this case, on the side of fluid a, invalidating a potential and incompressible flow model in that region of space. On the contrary, on side b, the tangential and normal velocities at the contact surface do not differ too much and hence an irrotational approximation works better, albeit not very far from the interface, where the vorticity field actually controls the spatial variations, as discussed in [7]. This behavior is a consequence of the distribution of vorticity generated by the rippled shock fronts. As the fronts moved away from the contact surface, the oscillations of their ripples amplitudes gave rise to a rotational steady state velocity field. Of course, in the very weak shock limit ($M_i - 1 \ll 1$), vorticity would be negligible in both gases and potential flow models for the asymptotic velocity fields would work reasonably well at both sides of the contact surface. Coming back to Fig. 3(c), we show the vorticity density map together with the streamlines associated to the velocity field. We can also track the zero crossings of the normal and tangential velocities in the vorticity density plot. On side b less vorticity is generated, as the reflected shock is generally weak in comparison to the incident shock. This fact is manifested not only by the magnitude of the vorticity itself, but also in the size of the vortices. The first vortex inside fluid b occupies a longitudinal extension of approximately one wavelength. On

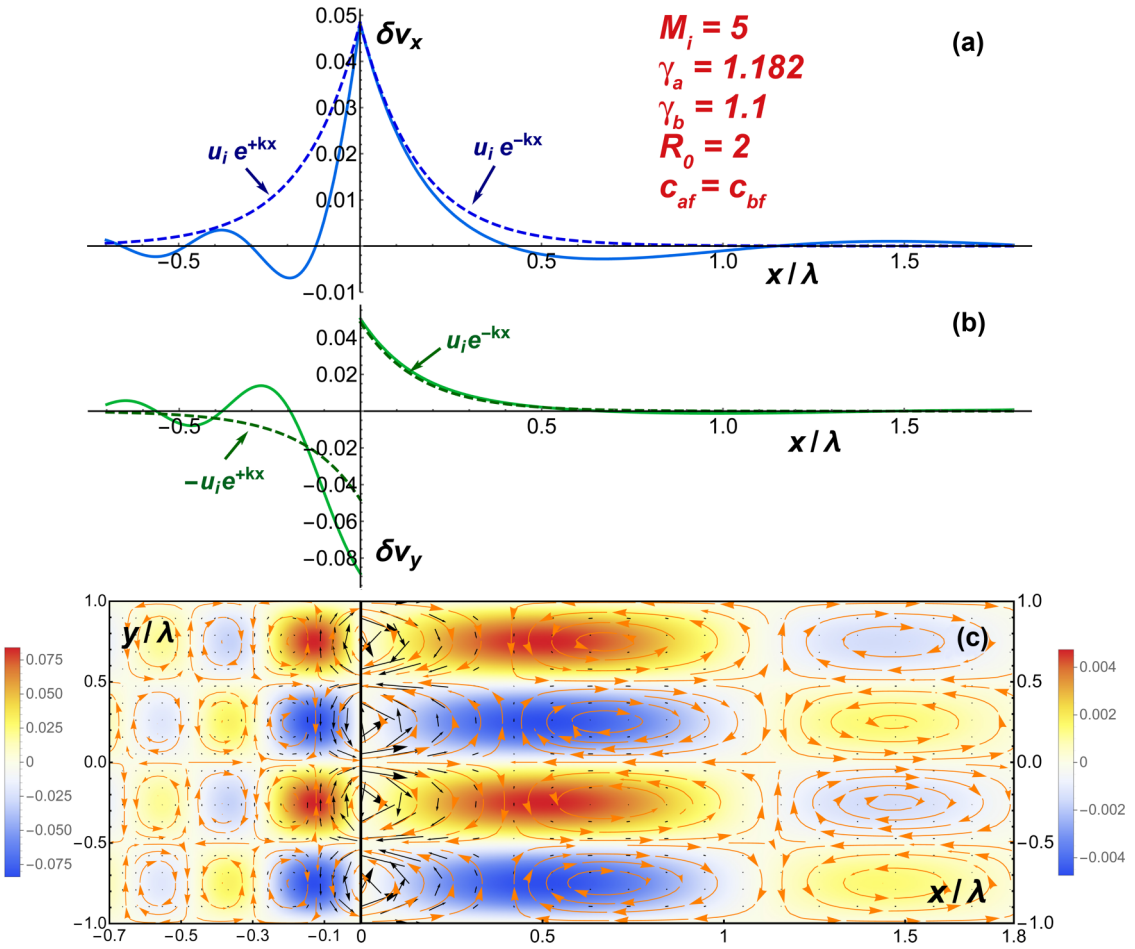

FIG. 3. Spatial profiles of the asymptotic normal velocity (a), tangential velocity (b), and a density map of the vorticity field (c) on which the streamlines have been superposed. The fluid parameters are shown inside the plot.

the contrary, inside fluid a, the amount of vorticity is larger and we can count up to almost four vortices within the same distance. We can visually track the maxima of $u(x)$ as zeros of $v(x)$ when comparing Fig. 3(a) with Fig. 3(b). Besides, we can also easily identify the zeros of the vorticity functions $g_a(x)$ and $g_b(x)$ in Fig. 3(c). The important quantities F_a and F_b are particular spatial averages of the vorticity profiles shown here. We can guess from the pictures shown that there can be significant amount of kinetic energy spread inside the fluids, in the form of rotational energy, associated with the vortices generated by the rippled fronts. Some interesting questions arise, as for example, how does this rotational kinetic energy scale with the four preshock parameters and how much of that energy is contained in the first two vortices, nearest to the contact surface? These questions will be addressed in a future work. Besides, the distribution of bulk vorticity at both sides of the contact surface may be important during nonlinear evolution of the ripple amplitude. In fact, as recent simulations indicate [25,26], there is only significant motion very near the interface in the nonlinear stage, probably inside the vortical structures generated by the rippled shock fronts during the period of linear growth [26]. Therefore, a precise quantification of the energy stored in them might be useful for the development of future nonlinear models.

D. Contact surface ripple growth

Experimental and simulation data are usually presented as plots of the interface ripple as a function of time. Recently, several simulations and experiments performed with gases have been reported and the data were shown as plots of $\psi_i(t)$, the interface corrugation, as a function of time [25–27,36,37]. In this subsection we present the predictions of our linear theory for the late time behavior of $\psi_i(t)$, within the interval of time during which linear theory is valid. A comparison with experiments and simulations will be presented in Sec. VI.

It is not difficult to see, using the tools of [11,15] and using the results of the previous paragraph, that the time evolution of the contact surface ripple can be followed since $t = 0+$, if we know the evolution of the pressure perturbations in each compressed fluid. The pressure perturbations can be calculated either by solving for the series of Bessel functions shown in Eqs. (22) and (23), as explained in [10], or calculating the inverse Laplace transforms of the functions $\tilde{P}$ and $\tilde{H}$, after suitable approximations for the functions F_{b2} and F_{a1} have been chosen, as explained in Appendix A. In any case, the results would be the same, independently of the method chosen to follow the dynamics of the perturbations. Increasing the Mach number would imply considering a larger number of terms inside the Bessel series expansion or iterating more times

when computing the functions F_{a1} and F_{b2}. The contact surface ripple can be followed in time with the help of the pressure perturbation function defined by the series of Bessel functions [Eq. (22)]. The dimensional contact surface velocity as a function of time ($t \geqslant 0+$), using the results of [10], is given by

$$\delta v_i(t) = k\psi_0 D_i u_i \int_{0+}^{kc_{bf}t} J_0(\tau)\, d\tau + k\psi_0 D_i \sum_{n=0}^{\infty} \omega_{2n+1}^{b} \times \left[J_{2n+1}(kc_{bf}t) + 2\sum_{k=0}^{n-1} J_{2k+1}(kc_{bf}t) \right], \quad (34)$$

and the amplitude of the contact surface ripple, as a function of time, is

$$\psi_i(t) = \psi_0^* + \int_{0+}^{t} \delta v_i(t')\, dt', \quad (35)$$

where

$$\psi_0^* = \left(1 - \frac{U}{D_i}\right)\psi_0 \quad (36)$$

is the postshock value of the compressed contact surface ripple amplitude at $t = 0+$.

It can be seen with the help of the Laplace transforms of the pressure perturbations that for very large times, the surface ripple grows asymptotically in the form

$$\psi_i(t \gg t_1) \cong \psi_\infty + \delta v_i^\infty t, \quad (37)$$

where δv_i^∞ is the dimensional value of the asymptotic linear growth rate, and ψ_∞ is an asymptotic ordinate whose value is theoretically given by

$$\psi_\infty = \psi_0^* - \frac{D_i}{c_{bf}}[F_{b1}'(0) - F_{b2}'(0)]\psi_0, \quad (38)$$

where the prime to the right of the functions F_{b1} and F_{b2} indicates the derivative with respect to the argument. The characteristic time t_1 indicated inside the argument of ψ_i in Eq. (37) marks the onset of the transition to the asymptotic stage within linear theory, and is also a fundamental quantity that must be evaluated as a function of the four preshock parameters. The analysis of the dependence of t_1 on γ_a, γ_b, R_0, and M_i is left for future research. A qualitative interpretation of ψ_∞ can be given after some algebra with Eq. (35). In fact, if we add and subtract δv_i^∞ inside the time integral, and consider very large times ($t \to \infty$), we obtain

$$\psi_\infty - \psi_0^* = \int_{0+}^{\infty} \left[\delta v_i(t) - \delta v_i^\infty\right] dt. \quad (39)$$

We show the result implied by the above equation as the shaded area between the curves given by $\delta v_i(t)$ and δv_i^∞ in Fig. 4(a).

If we define the dimensionless time $\tau_d = k\delta v_i^\infty t$ and plot the difference $[\psi_i(t) - \psi_\infty]/\psi_0$ as a function of τ_d, all the RM cases for which there is a reflected shock will collapse into a single straight line of slope 45°, for sufficiently large time, according to Eq. (37). This universal asymptotic behavior is shown in Fig. 4(b) for different choices of the mentioned quantities. For the cases shown in Fig. 4(b) we have chosen some of the experiments described in Sec. VI, as they encompass a wide range of initial density jumps, Mach numbers, and fluid compressibilities. Each curve $[\psi_i(t) - \psi_\infty]/\psi_0$ joins

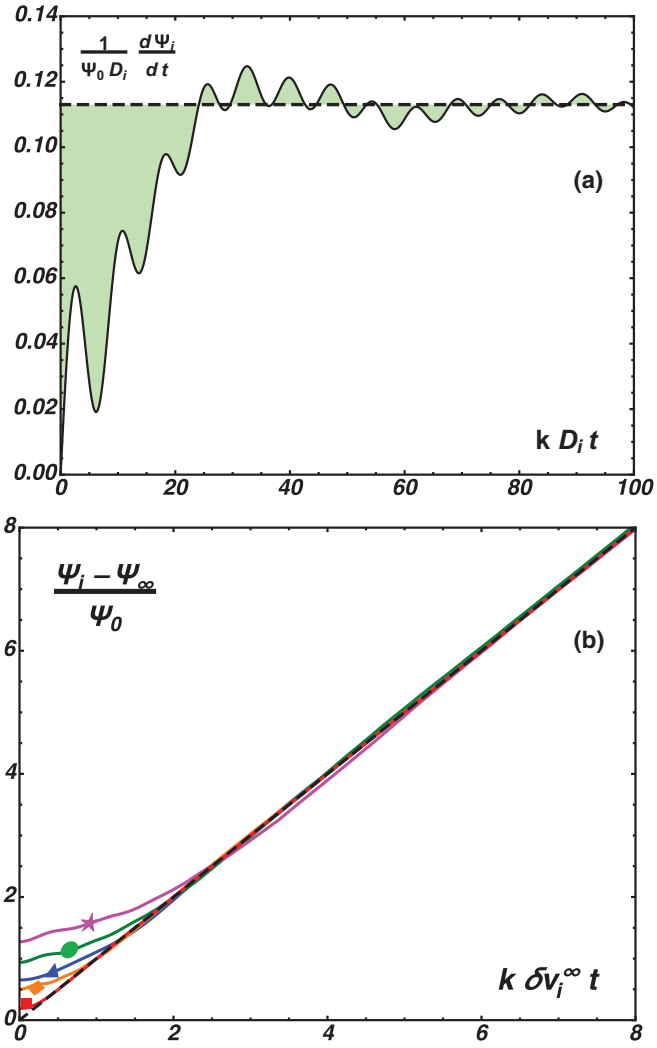

FIG. 4. (a) Temporal evolution of the contact surface ripple velocity for $\gamma_a = 1.0935$, $\gamma_b = 7/5$, $R_0 = 5.25$, and $M_i = 2.86$. The horizontal dashed line shows the asymptotic velocity $\delta v_i^\infty/(kD_i\psi_0)$. (b) Temporal evolution of the contact surface ripple corrugation $[\psi_i(\tau_d) - \psi_\infty]/\psi_0$ as a function of the dimensionless time: $\tau_d = k\delta v_i^\infty t$. Different choices of γ, R_0, and M_i are shown together. The markers correspond to different experiments in [36] and [37]: (1) magenta star: $\mathrm{He/SF_6}, R_0 = 39, M_i = 1.95$; (2) green circle: $\mathrm{He/SF_6}, R_0 = 39, M_i = 1.41$, (3) blue triangle: $\mathrm{air/SF_6}, R_0 = 5.23, M_i = 1.45$, (4) orange diamond: $\mathrm{He/SF_6}, R_0 = 39, M_i = 1.09353$, (5) red square: $(\mathrm{He} + \mathrm{Ar})/\mathrm{Ar}, R_0 = 1.817, M_i = 1.90$.

the universal asymptotic line τ_d at a different characteristic time, which we call τ_{d1} [related to the characteristic t_1 used in Eq. (37)]. In fact, the value of τ_{d1} is certainly a function of the four preshock parameters: γ_a, γ_b, R_0, and M_i. We see that τ_{d1} is different for each case. In fact, for the cases shown in Fig. 4(b), we can roughly estimate $\tau_{d1} \cong 3$ for case (1), $\tau_{d1} \cong 2$ for case (2), $\tau_{d1} \cong 1.5$ for case (3), $\tau_{d1} \cong 1$ for case (4), and $\tau_{d1} \cong 0.3$ for case (5). Nevertheless, as will be evident when we discuss the experiments of [36,37] in Sec. VI, the value of τ_{d1} might be also influenced by the ratio ψ_0/λ, because of nonlinear effects [37]. Besides, any real experiment will leave the asymptotic line depicted in Fig. 4(b) at a larger

characteristic time τ_{d2} due to nonlinearity, an ingredient that is obviously missing in Fig. 4(b). In an ideal situation in which the initial amplitude may be made arbitrarily small in comparison to λ, it would be $\tau_{d2} \to \infty$ as we make $\psi_0 \to 0$. We see that up to the value of $\tau_d \sim 6$ shown in Fig. 4(b), there are still small amplitude residual oscillations of the material surface ripple. They are essentially due to the late time sonic reverberations between the transmitted shock front and the contact surface and are stronger for the case with larger preshock density ratio, which corresponds to the case He/SF_6, with $R_0 = 39$ (Atwood number $A_T = 0.95$) and two values of incident Mach number: $M_i = 1.41$ and 1.95. These two cases take longer to enter into the theoretical asymptotic line in Fig. 4(b), because of the high density contrast at the contact surface and the high compressibility of the SF_6. These oscillations will be vanishingly small at larger times. As will be seen in the next section, the linear growth rate scales as $1/\sqrt{R_0}$ for a large density difference. Therefore, for very large preshock density ratios a finite value of τ_d would imply a very large dimensional time, as δv_i^∞ would be very small. To follow the surface ripple growth in these cases would imply adding a huge number of terms inside the series of Bessel functions [Eq. (22)] at the risk of increasing round-off errors. The complete temporal evolution of the surface ripples shown in Fig. 4(b) has been calculated with the help of the series indicated in Eq. (22), where we have used $n = 60$. The corresponding calculations to get the series coefficients are explained in [10]. This behavior will be discussed again in connection in Sec. VI with the experiments of [36,37].

Further, we realize that the value of ψ_∞, given by Eq. (38), is governed by the whole compressible evolution of the perturbations (since $t = 0+$). Its value depends on the derivative of $F_{b1} - F_{b2}$ evaluated at $q_b = 0$. This last fact makes it difficult to compute the asymptotic ordinate accurately, without enough iterations inside the functional equations that govern the pressure perturbations at the shock fronts. In Appendix C we explicitly show an iteration procedure to get accurate estimates of ψ_∞. The importance of the quantity ψ_∞ lies in the fact that it can be discerned experimentally as will be shown in Sec. VI, thus possibly becoming a useful diagnostic parameter in experiments where the equation of state (EOS) or constitutive properties of the compressed material might not be completely known in advance [19,22,30].

IV. APPROXIMATE FORMULAS FOR THE ASYMPTOTIC VELOCITIES

Normal asymptotic velocity: Irrotational approximation and high compression limit

The perturbed normal velocity at the contact surface, when the shocks are far enough in both fluids, is [Eqs. (31)]

$$u_i = \frac{\tilde{v}^0_{yb} - R\tilde{v}^0_{ya}}{R+1} + \frac{RF_a - F_b}{R+1}. \tag{40}$$

The first term is the contribution from the initial velocity shear deposited at the interface at $t = 0+$, just after the incident shock refraction. It is originated by the tangential velocities behind each rippled front in the compressed fluids. For very weak shocks, it is the only important contribution to the value of u_i. As it is obtained by neglecting the contribution from the bulk vorticities, we call it the *irrotational term* and write

$$u_{\text{irrot}} = \frac{\tilde{v}^0_{yb} - R\tilde{v}^0_{ya}}{R+1}. \tag{41}$$

We recall here that u_{irrot}, written in the previous equation, can also be obtained by reformulating the impulsive model, considering that the fluid elements suffer two different accelerations. Behind the transmitted front, fluid a is accelerated from 0 to U and behind the reflected shock, fluid b is accelerated from U_1 to U. This approach has been developed in [10] and the result is exactly the same as u_{irrot} above.

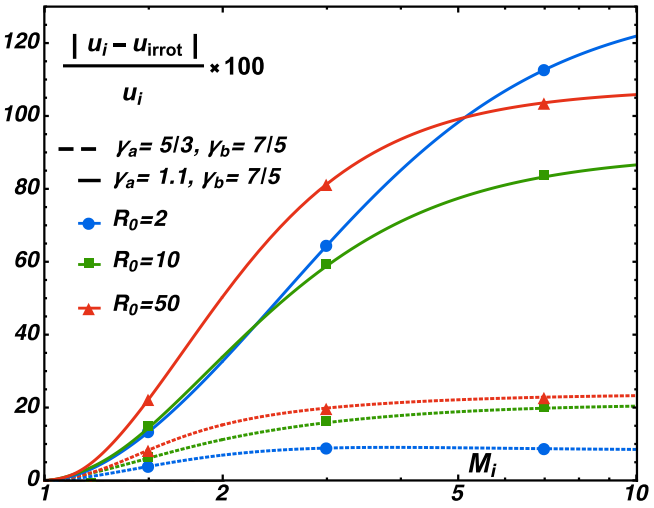

FIG. 5. Dependence of the relative difference between the exact growth rate and the irrotational approximation as a function of the incident shock Mach number.

We discuss in this section the goodness of an irrotational approximation to the asymptotic linear velocity in different domains of the space of parameters. We have at our disposal the exact solution u_i (obtained with the desired accuracy through a convenient number of iterations inside the functional equations) and the irrotational approximation provided by the same equations of fluids, the term named u_{irrot} above. As u_{irrot} can also be obtained with the reformulation of the impulsive model given in [11], the analysis that comprises Figs. 5, 6, 7, and 8 below can be seen as the analysis of the goodness of a potential flow model if it were used to calculate the perturbation normal velocity at the contact surface ripple. At the end of this section we present another approximate value for u_i, which consistently takes into account the true rotational nature of the perturbation fields left by the rippled shocks, and hence gives more accurate predictions, even at high compressions.

In Figs. 5, 6, 7, and 8, we compare the prediction of u_{irrot} with the complete solution obtained by iterating Eqs. (A5) until three significant digits are obtained for u_i (generally, five iterations is more than enough in all the cases). In Fig. 5, two sets of γ values are chosen: $\gamma_a = 5/3$, $\gamma_b = 7/5$ on one side, and $\gamma_a = 1.1$, $\gamma_b = 7/5$. The exact solution u_i is compared to u_{irrot} as a function of M_i for three values of the preshock density ratio: $R_0 = 2,10,50$. For the less compressible case ($\gamma_a = 5/3$), we see that the irrotational approximation is a good estimate of the normal velocity for the whole range of

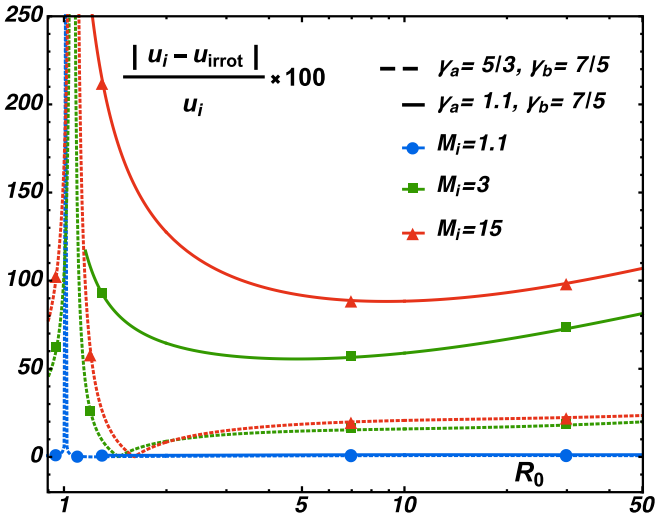

FIG. 6. Dependence of the relative difference between the exact growth rate and the irrotational approximation as a function of the preshock density ratio.

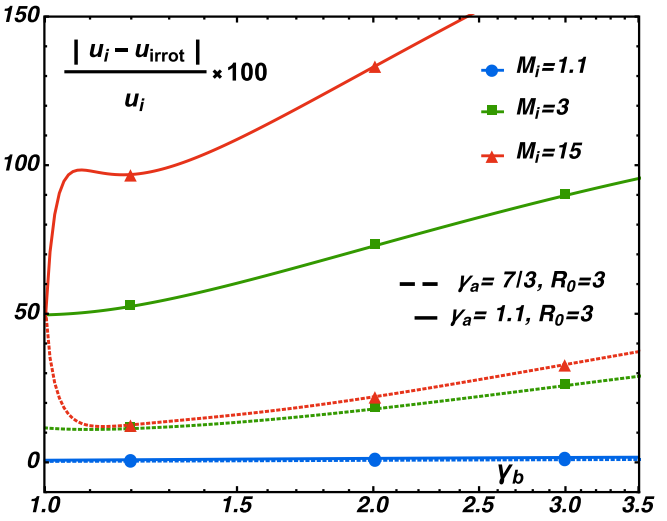

FIG. 8. Dependence of the relative difference between the exact growth rate and the irrotational approximation as a function of the isentropic exponent γ_b.

Mach numbers shown, and the relative error stays at most around 20% for the strongest incident shock. The situation is different for the second set of gases, where $\gamma_a = 1.1$ and $\gamma_b = 7/5$. The irrotational approximation gives a relative error which stays below 20% only for $M_i < 1.5$. At larger incident Mach number, the difference increases drastically.

In Fig. 6, the same two sets of gases are chosen but u_i is compared against u_{irrot} as a function of R_0 for different values of $M_i = 1.1,3,15$. For the weakest incident shock, agreement between the irrotational and complete solution is almost perfect in the whole range of preshock densities studied, for both sets of gases (with different compressibilities on the side of the transmitted shock), except for $R_0 - 1 \ll 1$ in the less compressible case, due to freeze-out, where the normal velocity is exactly zero [17,43]. As stronger shocks are considered, the disagreement worsens for the larger density ratios. This difference is more important as more compressible is the fluid on which the transmitted shock travels. Each curve shown in Fig. 6 ends to the left at the point $R_0 = R_0^m$ that marks the boundary between a reflected shock or a reflected rarefaction. The cases with $\gamma_a = 5/3$ have $R_0^m < 1$ and the cases with $\gamma_a = 1.1$ have $R_0^m > 1$. For the less compressible set of gases (where $\gamma_a = 5/3 > \gamma_b = 7/5$), the relative error stays below 25% even for the strongest shocks and at high density ratio. Besides, for this case, we have found a characteristic value of the preshock density ratio at which the relative error is zero, and increases again when decreasing R_0 still further towards the density ratio at which freeze-out occurs. At the freeze-out condition, the relative error grows unbounded [17,44]. For the more compressible case ($\gamma_a = 1.1 < \gamma_b = 7/5$), the relative error stays above 50% even for moderately strong shocks ($M_i = 3$) in the whole density range. As mentioned before, there is a curious behavior of the relative difference $u_i - u_{\text{irrot}}$ as a function of R_0 for the cases in which freeze-out is expected ($\gamma_a > \gamma_b$). We see that when R_0 decreases, there is a value at which $u_i = u_{\text{irrot}}$, because the bulk vorticity term $RF_a - F_b$ is exactly zero. This happens for all three Mach numbers studied in Fig. 6 at some value of R_0 near freeze-out. In particular, for the green dashed line ($M_i = 3$) we find that the bulk term vanishes at $R_0 \sim 1.450\ldots$. This is a surprising result, but it does not mean that the velocity fields are irrotational, because $F_{a,b}$ are different from zero ($F_a \sim 4.499\cdots \times 10^{-4}$, $F_b \sim 4.453 \times 10^{-4}$, and $R = 1.00689\cdots < R_0 = 1.451\ldots$). The vanishing of the bulk vorticity term occurs because F_a changes sign as R_0 decreases. In fact, for the same case as before, we find that $F_a = 0$ at $R_0 \sim 1.466\ldots$. It is worth adding that for these situations, $F_a \sim F_b$. As a consequence, there will be small regions of the parameter space, always in the vicinity of freeze-out conditions, in which $u_{\text{irrot}} < u_i$. This peculiar behavior is quite surprising, because it is opposed to the image we have had of the role of the bulk vorticity term.

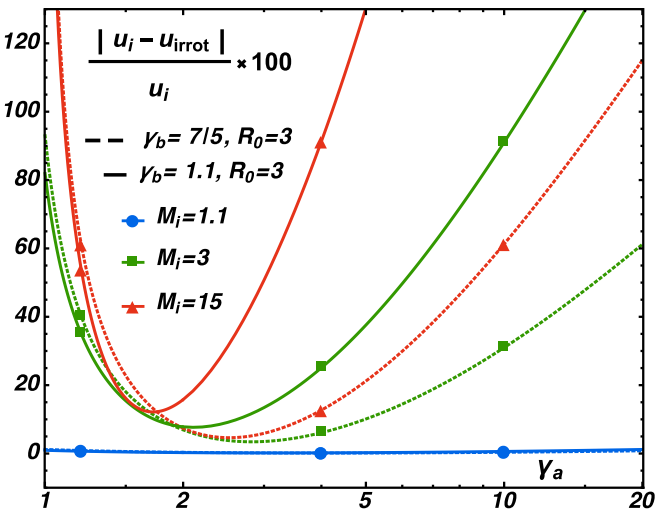

FIG. 7. Dependence of the relative difference between the exact growth rate and the irrotational approximation as a function of the isentropic exponent γ_a.

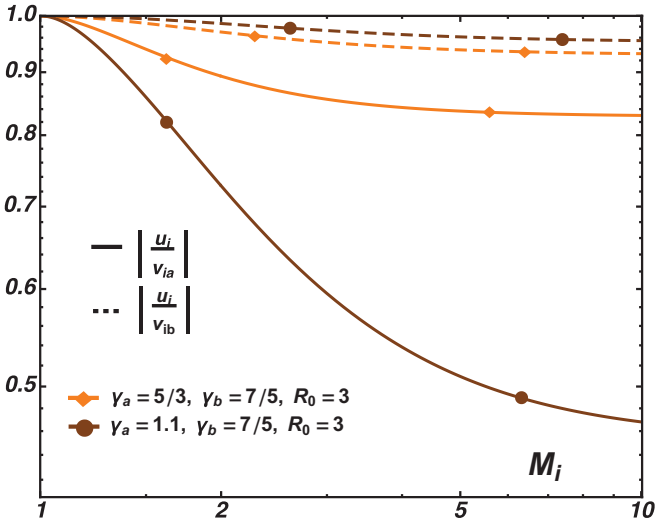

FIG. 9. Functional dependence of the velocity ratios $|u_i/v_{ia}|$ and $u_i/|v_{ib}|$ as a function of the incident shock Mach number M_i.

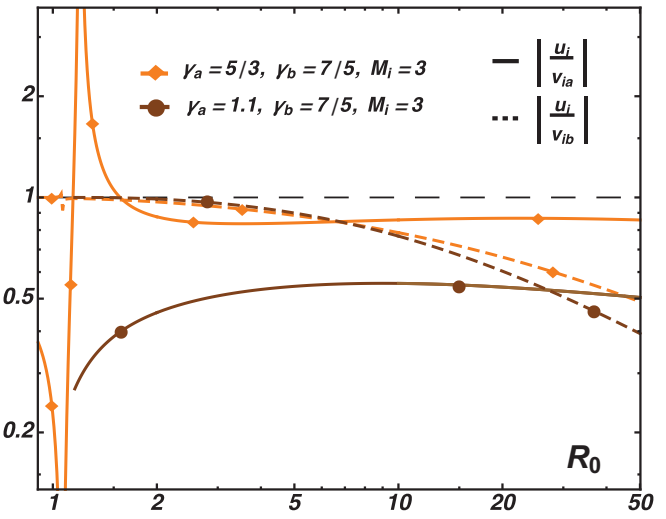

FIG. 10. Functional dependence of the velocity ratios $|u_i/v_{ia}|$ and $u_i/|v_{ib}|$ as a function of R_0.

This phenomenon is left for future study. For other regions of the space of parameters, which are not near freeze-out, we usually have $|F_a| \gg |F_b|$ and therefore, it is $u_i < u_{\text{irrot}}$.

In Fig. 7 the comparison is done as a function of γ_a for given values of $\gamma_b = 7/5$ and the preshock density ratio, $R_0 = 3$, for several values of the incident shock Mach number ($M_i = 1.1, 3, 15$). Of course, it might be impossible to find substances in nature that behave as ideal gases with isentropic exponents larger than 5/3. Nevertheless, there are situations of very incompressible materials that can be modeled by using large γ values. In any case, the aim of this comparison is to perceive the general trend as one of the fluids becomes less compressible. The agreement between u_i and u_{irrot} is excellent for $M_i = 1.1$ in the whole interval shown, due to the negligible generation of vorticity inside fluid a. However, for higher values of the incident Mach number, the approximation fails, except in a very narrow zone centered in the interval $1.5 < \gamma_a < 2.5$. For completeness, in Fig. 8 the comparison between u_i and u_{irrot} is done as a function of γ_b with given values of $\gamma_a = 1.1$, $R_0 = 3$ and is plotted for the same values of M_i. As in Figs. 5 and 6, the same distinguishing behavior is observed here when changing the value of γ_a. The difference increases when $\gamma_a = 1.1$. For very weak shocks ($M_i = 1.1$), the relative error is negligible in any case.

There is another criterion to decide whether an irrotational assumption is acceptable and comes from the comparison between the asymptotic tangential velocities at both sides of the material interface with the normal velocity. In Figs. 8, 9, 10, and 11, we show the values of $|u_i/v_{ia}|$ and $|u_i/v_{ib}|$ as a function of the four parameters, as we did with the normal velocity relative difference in Figs. 5–8. As expected, for situations in which bulk vorticity generation is not important, the absolute values of both tangential velocities are very similar and their values agree quite well with the normal velocity. This similarity is a signature of an almost irrotational velocity field in both fluids. In Fig. 9, the difference between both velocities increases at high Mach number for each pair of gases. Another perspective of the comparison is shown in Fig. 10, where the tangential velocities are plotted against R_0 for $M_i = 5$ and the same sets of gases as in Fig. 9. We see that the tangential velocities are almost equal to the normal velocity inside fluid b, because little vorticity is generated there. This is not true inside fluid a. We recognize a similar behavior to that in Fig. 6, when the preshock density reaches the freeze-out value or the minimum allowed value to have a shock reflected. For the case $\gamma_a = 5/3$, $\gamma_b = 7/5$, $M_i = 3$, we see that the ratio $|u_i/v_{ia}|$ reaches a maximum for $R_0 \cong 1.2$. This behavior is noteworthy, because it indicates that the transverse velocity in fluid a reaches a minimum. In fact, if we make a zoom near $R_0 = 1.2$ we obtain approximately $|u_i| \sim 10^{-2}$, $|v_{ib}| \sim 10^{-2}$, and $|v_{ia}| \sim 10^{-6}$. This means that when decreasing R_0 to reach the freeze-out boundary to the left, the asymptotic transverse velocity inside fluid a also decreases and reaches a minimum, which is not zero. This is probably related to the change of orientation of δv^0_{ya}, a necessary condition to achieve freeze-out [17,44]. In fact, $\delta v^0_{ya} < 0$ if $R_0 \gtrsim 1.382\ldots$

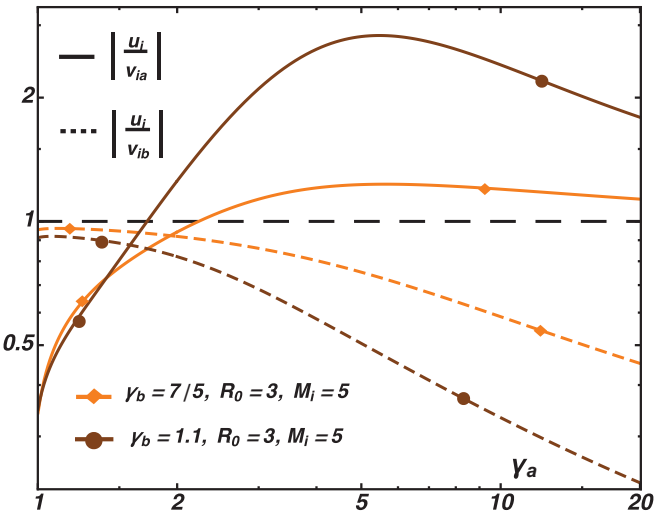

FIG. 11. Functional dependence of the velocity ratios $|u_i/v_{ia}|$ and $u_i/|v_{ib}|$ as a function of γ_a.

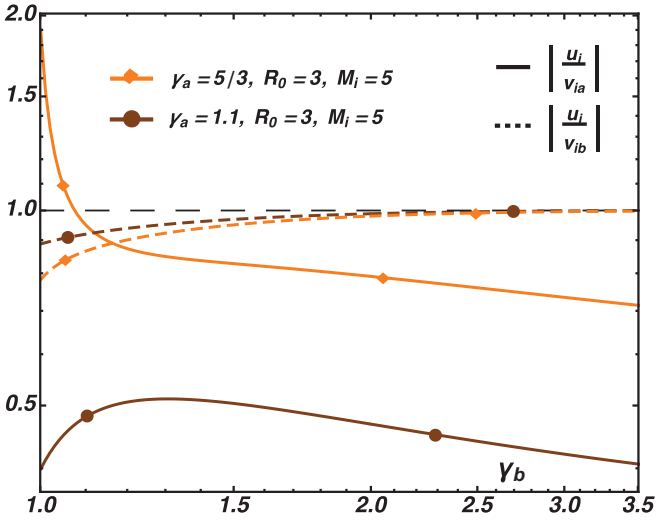

FIG. 12. Functional dependence of the velocity ratios $|u_i/v_{ia}|$ and $u_i/|v_{ib}|$ as a function of γ_b.

and $\delta v^0_{ya} > 0$ if $R_0 \lesssim 1.382\ldots$. On the contrary, v_{ib} does not show this curious behavior, probably because δv^0_{yb} is never zero when we change R_0. As is easily noticed, the situation just described can never occur in a purely irrotational velocity field. These conclusions emphasize the richness of the perturbed flows generated behind rippled shocks.

In Fig. 11 we compare v_{ia} and v_{ib} as a function of γ_a for $R_0 = 3$ and $M_i = 5$, for two values of $\gamma_b = 7/5$ and $5/3$. An irrotational assumption is acceptable for $\gamma_a \lesssim 2$ inside fluid b. Finally, in Fig. 12 the ratios $|u_i/v_{im}|$ are shown as a function of γ_b for specific choices of the other parameters: $\gamma_a = 5/3$ and $\gamma_a = 7/5$ for $R_0 = 3$ and $M_i = 5$. We easily realize that for the situations in which compressibility is not important ($\gamma_b \gg 1$), the velocity ratio tends to unity. As an important result, after looking at the dependencies shown in Figs. 5–12, we can conclude that an irrotational assumption for the velocity fields is perhaps more adequate inside fluid b, but not when compression is important in the other fluid. The potential flow hypothesis is even less justifiable inside fluid a, except for the regimes in which compressibility is not important.

Having shown that the irrotational approximation is of limited usefulness for arbitrary values of the preshock parameters, except for very weak shocks, it is is worth examining the possibility of using an approximate formula for u_i that can be extended beyond the domain of validity of $u_{\rm irrot}$. This is done by using the functions shown in Eqs. (33) which depend on the seed functions $F^{[0]}_{a1}$ and $F^{[0]}_{b2}$ of Eqs. (A7). In this form, we can write an approximate normal velocity that incorporates rough information of the bulk vorticity profile, and which we call $u^{[0]}_i$:

$$u^{[0]}_i = \frac{\tilde{v}^0_{yb} - R\tilde{v}^0_{ya}}{R+1} + \frac{RF^{[0]}_a - F^{[0]}_b}{R+1}. \tag{42}$$

In Fig. 13(a) we compare u_i with $u^{[0]}_i$ for $\gamma_a = 5/3$, $\gamma_b = 7/5$, and two values of $R_0 = 2$ and 5 as a function of the incident shock Mach number. The same is done in Fig. 13(b) where $\gamma_a = 1.1$. For the first case, we see that $u^{[0]}_i$ gives a good estimate of the normal velocity in the whole range studied

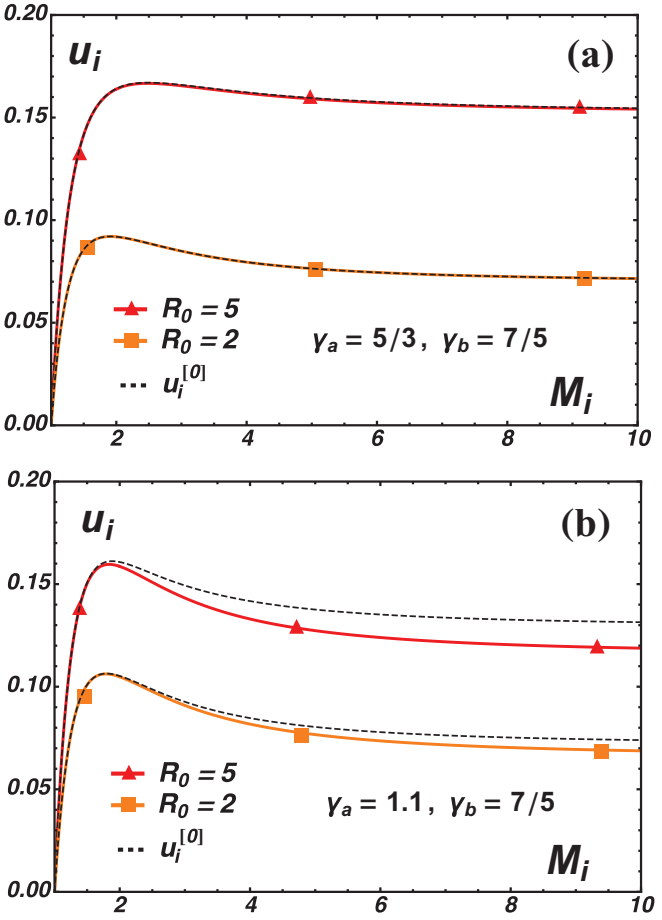

FIG. 13. Comparison between the exact value of u_i (obtained with at least five iterations) and the approximate formula Eq. (42) (without iterations) for (a) $\gamma_a = 5/3$ and (b) $\gamma_a = 1.1$.

here: $1 \leqslant M_i \leqslant 10$. The difference between them is not very dependent on the values of R_0. However, for the second case, when fluid a is more compressible, there is a small difference in the strong shock regime, which increases if R_0 increases. The general trend observed is that for high compression situations, more iterations are needed and the starting value $u^{[0]}_i$ might not be accurate enough. Each iteration round improves in taking into account the effect of the reverberation of sound waves between the rippled fronts and the contact surface. The reverberations become more important as R_0 increases because as the density of fluid a increases, the relative velocity of the transmitted shock with respect to the contact surface decreases. Therefore, both surfaces are interacting for a longer period of time which makes it necessary to consider more iterations in the functional equations written in Eqs. (A5).

V. APPROXIMATE VALUES OF THE ASYMPTOTIC VELOCITY IN DIFFERENT PHYSICAL LIMITS

A. Weak shock limit ($M_i - 1 \ll 1$)

1. *Taylor expansion of the normal ripple velocity*

When the incident shock Mach number is very near unity, the irrotational term gives a good estimation of the normal and tangential velocities. But as the shock intensity increases, the

bulk vorticity term becomes important. With this objective in mind, we expand u_i in powers of $M_i - 1$. We therefore expand u_{irrot} and also the bulk term composed by the parameters F_a and F_b. Instead of expanding the functional equations, it is more convenient to follow the strategy used in [39] in the same limit. In fact, we realize from Eq. (29) that we formally need the Laplace transforms $\tilde{P}_t(-\chi_t)$ and $\tilde{P}_r(\chi_r)$. We write Eq. (29) here again, as it is necessary for our discussion:

$$F_a = -\Omega_a \sinh \chi_t \tilde{P}_t(q_a = -\chi_t),$$
$$F_b = -\Omega_b \sinh \chi_r \tilde{P}_r(q_b = \chi_r). \tag{43}$$

We notice by taking the Laplace transform in the domain of the variable r in Eq. (22) that we can always write the following formal series for any of the fluids ($m = a$ or $m = b$) [39]:

$$\tilde{P}_m(s) = \sum_{n=1}^{\infty} \frac{\tilde{p}_{m0}^{(2n+1)}}{s^{2n}}, \tag{44}$$

only valid within its circle of convergence in the complex plane. The coefficient $\tilde{p}_{m0}^{(2n+1)}$ is the $(2n+1)$th derivative of the pressure perturbation (with respect to the coordinate r) evaluated at $t = 0+$. The explicit analytical dependencies of the first and third initial derivatives are shown in the Supplemental Material [41], for the purpose of completeness. It is easy to see that higher derivatives would soon become very involved functions of the pre- and postshock flow quantities.

We expand Eq. (40) up to order $(M_i - 1)^4$ and obtain, after some algebra,

$$u_i \cong a_1(M_i - 1) + a_2(M_i - 1)^2 + a_3(M_i - 1)^3 + a_4(M_i - 1)^4 + O[(M_i - 1)^5], \quad M_i - 1 \ll 1. \tag{45}$$

We only show here the coefficients a_1 and a_2:

$$a_1 = \left(\frac{R_0 - 1}{R_0 + 1}\right) \frac{8 y_F}{(\gamma_b + 1)(y_F + 1)},$$
$$a_2 = \frac{4 P_w(\gamma_a, \gamma_b, R_0)}{\gamma_a \gamma_b (\gamma_b + 1)^2 (R_0 + 1)^2 (y_F + 1)^3}, \tag{46}$$

where $y_F = \sqrt{\gamma_b/(\gamma_a R_0)}$ is the same quantity as the parameter y defined by Fraley after his Eq. (48) in Ref. [7]. The polynomial P_w is

$$\begin{aligned} P_w(\gamma_a, \gamma_b, R_0) &= 8\gamma_a^2 R_0(R_0 + 1) y_F - 8\gamma_a^2 R_0(3R_0 - 1) y_F^2 \\ &- \gamma_a^2 R_0\left(23R_0^2 + 40R_0 - 15\right) y_F^3 \\ &- 2\gamma_a^2 R_0\left[2(\gamma_a + 1)R_0^3 - 7R_0^2 - 2(\gamma_a - 1)R_0 - 5\right] \\ &\times y_F^4 - \gamma_a^2 R_0\left(7\gamma_a R_0^3 - 33R_0^2 - 7\gamma_a R_0 + 1\right) y_F^5 \\ &- 2\gamma_a^3 R_0^2\left(R_0^2 - 1\right) y_F^6 + \gamma_a^3 R_=^2\left(R_0^2 - 1\right) y_F^7. \end{aligned} \tag{47}$$

The coefficients a_3 and a_4 involve increasingly larger expressions. See the Supplemental Material [41] for the weak shock expansion coefficients. We see that a_1 is proportional to the ratio $(R_0 - 1)/(R_0 - 1)$. The proportionality with $(R_0 - 1)/(R_0 - 1)$ does not hold if we increase the shock strength such that the second term, proportional to $(M_i - 1)^2$, becomes important. The coefficient a_1 is zero when $R_0 = 1$, independently of the values of γ at both sides of the contact surface. If $R_0 = 1$ and $\gamma_a \neq \gamma_b$, the coefficient a_2 is not zero, and therefore, the asymptotic velocity is proportional to $(M_i - 1)^2$ in the weak shock limit for different fluids with equal preshock densities. However, for equal γ's in that case, a_2 is zero, as it should be. It is noted that retaining up to the second coefficient a_2, no information is present in it about the bulk vorticity profiles. The coefficients a_1 and a_2 correspond to the Taylor series expansion of the irrotational component of the asymptotic velocity [Eq. (41)]. It is adequate here to compare with the expansion shown in Ref. [7] in the same limit. Fraley derived a second order expansion in the parameter $\epsilon = (p_1 - p_0)/p_1$. It is related to our parameter z_i through $z_i = \epsilon/(1 - \epsilon)$. Besides, Fraley normalized the asymptotic velocity at the material interface with respect to $k\psi_0 U$, where U is the zero order velocity of the material surface, defined in Eq. (7). We can compare his results with ours by expanding the corresponding expressions in powers of ϵ. We expand Eq. (45), but using U instead of D_i to normalize the growth rate, and get

$$\frac{\delta v_i^{\infty}}{k\psi_0 U} \cong \frac{R_0 - 1}{R_0 + 1} + a_{F1}\epsilon + a_{F2}\epsilon^2 + a_{F3}\epsilon^3 + O(\epsilon^4), \quad \epsilon \ll 1, \tag{48}$$

where the coefficient a_{F1} is given by

$$a_{F1} = \frac{\gamma_a R_0^2 Q_F}{2\gamma_a^3 y_F^4 (y_F + 1)^2 R_0^2 (R_0 + 1)^2} \tag{49}$$

and the polynomial Q_F is given by

$$\begin{aligned} Q_F(\gamma_a, \gamma_b, R_0) &= 2(R_0 + 1) - 2(3R_0 - 1) y_F \\ &- 2(R_0 + 2)(3R_0 - 1) y_F^2 - \left(R_0 - 1 - \gamma_a R_0\right. \\ &\left. - 5R_0^2 + R_0^3 + \gamma_a R_0^3\right) y_F^3 - \left(R_0 + 1 - \gamma_a R_0\right. \\ &\left. - 9R_0^2 - R_0^3 + \gamma_a R_0^3\right) y_F^4 + \gamma_a R_0\left(R_0^2 - 1\right) y_F^5 \\ &+ \gamma_a R_0\left(R_0^2 - 1\right) y_F^6. \end{aligned} \tag{50}$$

We have only shown the coefficient a_{F1} in the last equation. The coefficients a_{F2} and a_{F3} can be calculated using the expansions shown previously. Fraley had only shown an expansion up to the second term (which is linear in ϵ after normalizing by $k\psi_0 U$). The coefficient he showed does not agree with our a_{F1}. Retaining up to a_{F1} does not include bulk vorticity effects and its extrapolation for stronger shocks would not be correct. We see that the first term of Eq. (48) is just the preshock Atwood number, in agreement with Fraley and with Richtmyer's prescription for the impulsive model [5,7]. In fact, the impulsive model formula is

$$\delta v_{\text{imp}} = U\left(\frac{R_0 - 1}{R_0 + 1}\right) k\psi_0, \tag{51}$$

which is, formally speaking, the lowest order contribution to the growth rate in powers of $M_i - 1$. Richtmyer arrived at this result by generalizing the Rayleigh-Taylor growth rate for the case of a very high gravity acceleration acting for a vanishingly small amount of time. He also suggested extending this result, for stronger shocks, using the postshock values of the density ratio at the interface ($R = \rho_{af}/\rho_{bf}$) as well as the postshock value of the initial ripple amplitude:

$$\delta v_{\text{imp}}^{*} = U\left(\frac{R - 1}{R + 1}\right)\left(1 - \frac{U}{D_i}\right) k\psi_0. \tag{52}$$

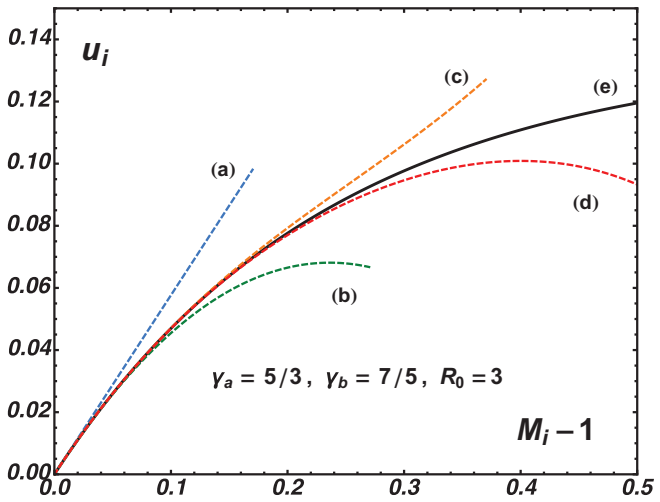

FIG. 14. Comparison between the exact normal velocity u_i as a function of the shock strength with the different terms of the expansion shown in Eq. (45). Curve (a) represents the first, linear term: $a_1(M_i - 1)$, curve (b) includes up to the second power: $a_1(M_i - 1) + a_2(M_i - 1)^2$, curve (c) up to the third: $a_1(M_i - 1) + a_2(M_i - 1)^2 + a_3(M_i - 1)^3$, curve (d) up to the fourth term: $a_1(M_i - 1) + a_2(M_i - 1)^2 + a_3(M_i - 1)^3 + a_4(M_i - 1)^4$, and (e) is the exact value.

Nevertheless, this last form of the impulsive formula, even though it may appeal to intuition because it is obtained substituting R_0 and ψ_0 by their postshock values, is not predicted by the rigorous linear theory. This fact has been amply discussed in [43], when studying the possibility of zero asymptotic normal growth for weak shocks. As the shock strength increases, higher order terms of the expansion become important and, rigorously speaking, the normal velocity is no longer proportional either to the preshock Atwood number or to its postshock value.

In Fig. 14 we show the normal velocity u_i for a given pair of gases ($\gamma_a = 5/3$, $\gamma_b = 7/5$, $R_0 = 3$) as a function of M_i. We show the exact result, obtained with the complete Eq. (40) and the different degrees of approximation indicated in Eq. (45). We see that very little is gained by adding successive terms. We have included up to the fourth-order term and the agreement with the exact solution is good for $M_i \lesssim 1.3$. Adding more terms does not improve the comparison at larger Mach numbers and the calculation cost is enormous. As already seen in Ref. [39], the weak shock expansion series is only useful within its circle of convergence. Our experience is that this circle of convergence decreases very fast when compressibility becomes important. It is not difficult to realize this fact by noting that the series given by Eq. (44) must be evaluated inside both fluids. Inside fluid a, the quantity $1/|\sinh \chi_t|$ may become a number larger that unity, indicating that the corresponding series may be divergent. Besides, as it is almost impossible to deduce a general analytical trend for the derivatives $\tilde{p}_{m0}^{(2n+1)}$, the usual convergence tests are ruled out. Hence, we can only compare expansions such as Eq. (45) with the exact solution for particular cases. As a general rule, we have verified that weak shock expansions of the type discussed here are not useful for, approximately, $M_i \gtrsim 1.3$. A conclusive answer regarding the exact convergence radius could be given if the analytical solution to the postshock flow quantities could be written explicitly. In such a situation, the function u_i could then be studied in the complex plane for complex values of the arguments: γ_a, γ_b, R_0, and M_i. The singularity with the smallest absolute value in the complex plane would determine the circle of convergence, as also discussed in another context in [35]. So far, no such analytic solutions for the postshock quantities have been reported and, therefore, the precise calculation of the corresponding singularities still remains an open problem and is out of the scope of the present work.

2. *Freeze-out in the weak shock limit*

As mentioned in previous sections, the interaction between the transmitted and reflected shocks with the corrugated material surface may result in certain special situations where the normal asymptotic velocity is zero in linear theory. This phenomenon has been initially studied by Mikaelian in the context of shock compression of thermonuclear targets, aimed at reducing the initial degree of nonuniformity of the imploding shell and named the phenomenon single interface *freeze-out* [42,43]. Long before that, he used a similar name in another context where a second shock cancels the effect of a first shock [45]. We refer here to freeze-out as the set of conditions for which the asymptotic normal velocity at the contact surface ripple is exactly zero, when dealing with a single incident shock. It was initially studied with the the impulsive model looking for situations in which the postshock Atwood number could be zero [42,43]. Because the impulsive model prescription given by Eq. (52) failed, Mikaelian attacked the problem with Fraley's fully compressible model, using his Taylor expansion of the growth rate. In this way, Mikaelian obtained for the first time an approximation to the freeze-out contour curves, showing that different γ values at both sides of the interface is a necessary requisite [43]. Much later, the same problem was studied again, including the effects of the vorticity generated by the shocks inside the compressed fluids, either for a shock or a rarefaction reflected [17,44]. Even though the shock reflected situation was studied with some detail in [17], an exact explicit Taylor expansion of the freeze-out contour curves in the weak shock limit was not given in that work. This can be easily done here, using the Taylor expansion shown in Eq. (45). In fact, at freeze-out, the contour curve would be defined by a formula such as

$$R_0 = e_0 + e_1(M_i - 1) + e_2(M_i - 1)^2 + e_3(M_i - 1)^3 + O[(M_i - 1)^4], \quad M_i - 1 \ll 1, \tag{53}$$

where the coefficients e_0, e_1, etc., are only functions of γ_a and γ_b. We substitute the above expression inside Eq. (45) and equate to zero. It is not difficult to see that $e_0 = 1$. Because of lack of space, we only show here the coefficients, e_1 and e_2. The coefficient

e_3 is a rather long expression and can be found in the Supplemental Material [41]:

$$e_1 = -4\frac{\gamma_a + 2\gamma_b - 3\sqrt{\gamma_a\gamma_b}}{(\gamma_b+1)\sqrt{\gamma_a\gamma_b}},$$

$$e_2 = \frac{2}{\gamma_b+1}\left\{\frac{\sqrt{\gamma_a}-\sqrt{\gamma_b}}{\gamma_a(\sqrt{\gamma_a}+\sqrt{\gamma_b})}\left[\left(4\gamma_a^2 - 7\gamma_a\gamma_b - 28\gamma_b^2 - 11\gamma_b^2\right) + \left(-9\gamma_a + 7\gamma_a\gamma_b + 32\gamma_a\gamma_b - 4\gamma_b^2\right)\sqrt{\gamma_a\gamma_b}\right]\right.$$
$$\left. - \frac{\gamma_a + 2\gamma_b - 3\sqrt{\gamma_a\gamma_b}}{\sqrt{\gamma_a\gamma_b}}\right\}. \tag{54}$$

It can be verified that the above coefficients are zero when $\gamma_a = \gamma_b$. A comparative plot between the curve given by Eq. (53) and the exact contour curve is shown in the weak shock limit for two different pairs of ideal gases, in Fig. 15. Because the approximate expression is derived from the Taylor expansion of the growth rate, the formula given by Eq. (53) shows a similar behavior to that in Eq. (45). The approximate expansion is only useful within its circle of convergence, making it inappropriate at larger values of M_i, in general. There is another interesting conclusion when examining Eq. (53): all the freeze-out contours in the weak shock limit start at the point $(M_i, R_0) = (1,1)$. A similar behavior has been observed in [44] for freeze-out when a rarefaction is reflected. We would be tempted to think that the freeze-out contours in the weak shock limit might start nearer the boundary of total transmission with an initial ordinate R_0^m. That this would never be possible can be qualitatively understood from the situation at the contact surface at $t = 0+$ [see, for example, Fig. 1]. At total transmission, the tangential velocity on side b is equal to zero, because $U_1 = U$ and there is no reflected shock. Thus, the contact surface ripple is continuously "bombarded" with sonic perturbations that come from the transmitted shock but there are no such perturbations coming from inside fluid b to balance them. This means that the pressure perturbations emitted by the transmitted shock are not counteracted by a similar train of pressure waves coming from the right. As a result, there is a net pressure gradient due to the influence of the transmitted front, and then the asymptotic normal growth cannot be made zero. The important conclusion of this discussion is that any freeze-out contour that connects with the weak shock limit will always start at the point $(M_i, R_0) = (1,1)$. We do not know whether there are freeze-out contours that start from a different initial point, disconnected from $(M_i, R_0) = (1,1)$. Those regions might not be excluded *a priori*, for example, in the strong shock limit (as happens for the case of a rarefaction reflected, discussed in [14,44]), but their search is outside the scope of the present work and is left for future research.

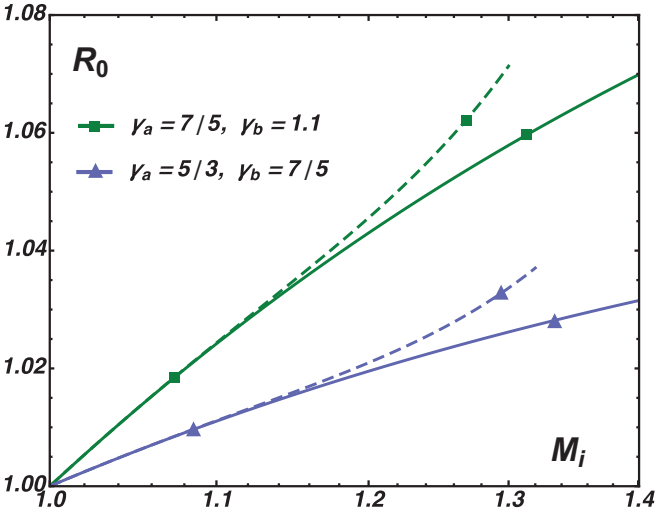

FIG. 15. Comparison between the exact freeze-out contour curve (obtained according to formalism developed in [17]) and the Taylor expansion shown in Eq. (53). The solid curves give the exact values of (M_i, R_0) at which freeze-out is expected for that choice of isentropic exponents. The dashed curves represent the approximate estimates according to the Taylor expansion of Eq. (53).

Besides, it is noted that if we only consider the coefficient e_1, no information on the bulk vorticity would be included, because the $F_{a,b}$ parameters are of third order in the weak shock limit. However, the coefficient e_1 contains exact information on u_{irrot}. Hence, a potential flow model of the RM velocity field would only give the initial slope of the contour curve. The contours given by Eq. (53) are accurate up to order $(M_i - 1)^3$, which means that the effect of the vorticity spread at both sides of the contact surface is taken into account. It is immediate that Eq. (53) above is equivalent to Eq. (9) of [44].

B. Strong shock limit ($M_i \gg 1$)

We now discuss the expansion of the normal velocity in powers of $1/M_i$:

$$u_i = b_0 + \frac{b_2}{M_i^2} + O\left(\frac{1}{M_i^4}\right). \tag{55}$$

The coefficients of the above expansion are only shown in the MATHEMATICA [46] files attached to this work, in case the reader is interested in working with them (see the Supplemental Material [41]). The analytical expressions are rather cumbersome and are several pages long to write. The coefficients of the expansion are calculated without iteration. That is, the above expression is actually the expansion of $u_i^{[0]}$. Adding the next iteration step would have resulted in much larger expressions to be analytically handled by the mathematical software in a reasonable amount of time. As can be seen from Fig. 16, expanding the expression of $u_i^{[0]}$ gives reasonable accuracy from moderate to strong shocks. Discrepancies on the order of 10% are seen when the fluid behind the transmitted shock is highly compressible.

In Fig. 16 we show two different cases: $\gamma_a = 5/3, \gamma_b = 7/5, R_0 = 3$ and $\gamma_a = 1.1, \gamma_b = 7/5, R_0 = 5.25$. This last case is taken from the experiments of [36]. We see that the

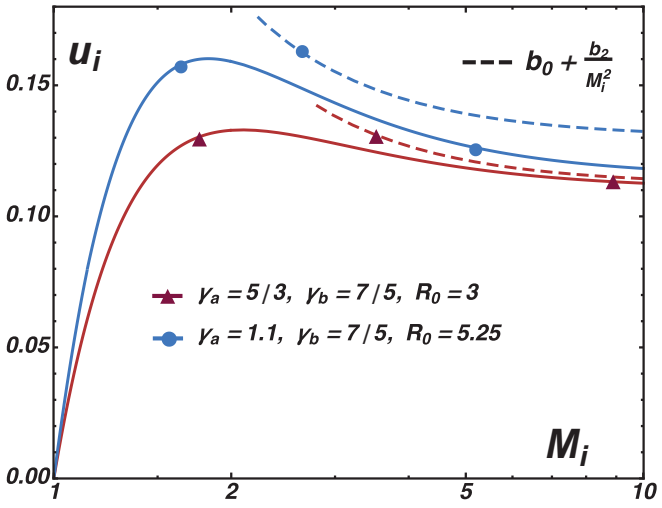

FIG. 16. Comparison between the exact normal velocity u_i and Eq. (55) valid at large values of M_i.

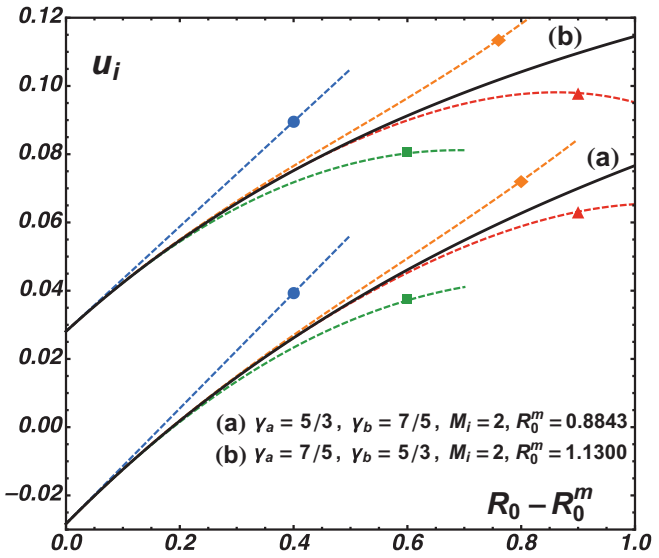

FIG. 17. Comparison between the exact normal velocity u_i and the Taylor expansion shown in Eq. (56) as a function of the variable $R_0 - R_0^m$. Each dashed line refers to a particular order of the expansion: blue circles represent the linear term, the green square includes up to the quadratic term, the orange diamond includes up to the cubic term, and the red triangle up to the quartic term.

agreement between the exact solution (solid curve) and the expansion (dashed curve) is better when fluid a is less compressible.

C. Small preshock density ratio ($R_0 - R_0^m \ll 1$)

It is possible to get accurate analytical expansions for situations in which the preshock density ratio is very near the minimum value required to have a reflected shock ($R_0 - R_0^m \ll 1$). When R_0 approaches R_0^m the reflected shock strength decreases towards $M_r = 1$. For $R_0 < R_0^m$ we would get a rarefaction reflected. The value of R_0^m is given by Eq. (11). Therefore, it looks feasible to make an expansion of the ripple's normal velocity in powers of $R_0 - R_0^m$, when this quantity remains small enough. We expand the expression given for $u_i^{[0]}$ up to fourth order in the difference $R_0 - R_0^m$ and obtain an expression of the form

$$u_i = c_0 + c_1\left(R_0 - R_0^m\right) + c_2\left(R_0 - R_0^m\right)^2 + c_3\left(R_0 - R_0^m\right)^3 + c_4\left(R_0 - R_0^m\right)^4 + O\left[\left(R_0 - R_0^m\right)^5\right],\ R - R_0^m \ll 1. \tag{56}$$

See the Supplemental Material [41] for the analytical expressions of the coefficients c_0, c_1, c_2, c_3, and c_4. In Fig. 17 we show a comparison between retaining successive terms of the above expression with the exact solution for two particular cases: $\gamma_a = 5/3,\ \gamma_b = 7/5,\ M_i = 2,\ R_0^m \cong 0.8842\ldots$ and $\gamma_a = 7/5, \gamma_b = 5/3, M_i = 2, R_0^m \cong 1.1299\ldots$. The case with $\gamma_a = 5/3$ shows freeze-out at a definite preshock density ratio $R_0 > R_0^m$. On the other hand, no freeze-out is observed for the case studied with $\gamma_a = 7/5$. As has been observed before, when dealing with the expansion in powers of $M_i - 1$ in the weak shock limit, we also see a small convergence radius in the series implied by Eq. (56). This is probably due to the existence of a singularity in the complex plane associated with the dependence of u_i as a function of R_0. For the two cases shown in Fig. 17, the convergence limit seems to be inside the interval $R_0 - R_0^m < 0.5$. Of course, the exact determination of this boundary as an accurate function of the other parameters (γ_a, γ_b, and M_i) is out of the scope of the present work. Some years ago, Griffond has published the analysis of the growth at low Atwood numbers in [47], where the limit $R_0 - 1 \ll 1$ was considered, at the expense of dealing with fluids with equal γ values. In our case, the theoretical model used here allows the analysis of the perturbation growth starting at a different point in the parameter space, approaching the boundary of total transmission, thus considering fluids with different compressibilities. On the other hand, the analysis of [47] was not a Taylor expansion, like Eq. (56).

It is worth considering here again the discussion on freeze-out, in connection with Eq. (56) above. There is an important distinction between the expansions given by Eq. (56) and Eq. (45). When imposing the condition $u_i = 0$ on Eq. (45) we have obtained the freeze-out contours given by Eq. (53) in the weak shock limit, and all those contours invariably start at the point $(M_i, R_0) = (1,1)$. On the contrary, no such constraint is implied in the expansion given by Eq. (56), where the incident shock Mach number is, in principle, arbitrary. This leaves open the possibility of equating Eq. (56) to zero and deriving corresponding freeze-out contours that would not be necessarily topologically linked to the point $(M_i, R_0) = (1,1)$, as happens in Fig. 15. Given that the condition $M_i - 1 \ll 1$ is not a constraint in Eq. (56), this procedure unveils the opportunity of studying new regimes of freeze-out in the strong shock limit. Of course, this possibility is left for future study as it is well beyond the scope of this work.

D. Large initial density ratio ($R_0 \gg 1$)

If $R_0 \gg 1$, it is clear that u_i would be vanishingly small, because we would be reaching the rigid piston limit [39]. Therefore, we should expect a monotonic decrease of the normal velocity as the density ratio increases too much above

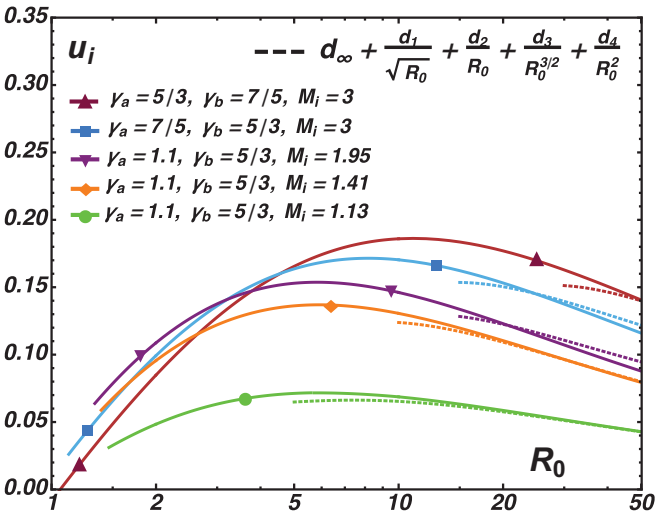

FIG. 18. Comparison between the exact normal velocity u_i and Eq. (57), valid at large values of R_0.

unity. The following expansion is proposed here to study this limit:

$$u_i = d_\infty + \frac{c_1}{R_0^{1/2}} + \frac{d_2}{R_0} + \frac{d_3}{R_0^{3/2}} + \frac{d_4}{R_0^2} + O\left(\frac{1}{R_0^{5/2}}\right). \quad (57)$$

We calculate the coefficients of the above expression by expanding the quantity $u_i^{[0]}$ in powers of $1/R_0$ (see Fig. 18). Because of this approximation, we get $d_\infty \neq 0$. Iterating an infinite number of times would make $d_\infty \to 0$. Despite this approximation, the formula shown in Eq. (57) is quite accurate for $R_0 \leqslant 50$. Of course, for much larger values of R_0 we would need to expand $u_i^{[n]}$ with larger values of the iteration index n. The interesting conclusion is that for very large values of R_0, the normal velocity would scale as $\sim 1/\sqrt{R_0} \sim \sqrt{1 - A_T}$, where A_T is the preshock Atwood number. See the Supplemental Material [41] for the analytical expressions of the coefficients of the above series. They are extremely large and therefore are not written here. In Fig. 17 we show a comparison between the exact value and the expansion of Eq. (57) for different choices of the preshock parameters: $\gamma_a = 5/3, \gamma_b = 7/5, M_i = 3$, $\gamma_a = 7/5, \gamma_b = 5/3, M_i = 3$; and we also show three cases taken from the experiments of [36]: $\gamma_a = 1.1$ and $\gamma_b = 7/5$ with three choices of the incident shock Mach number: $M_i = 1.13$, 1.41, and 1.91. The mentioned experiments are discussed in the next section.

VI. COMPARISON WITH SIMULATIONS AND EXPERIMENTS

It is worth discussing here the agreement observed between the results of this work and recently published 2D numerical simulations and experiments with ideal gases.

A. Numerical simulations

Regarding numerical simulations, the calculations carried out in [24–27] have compared favorably well with the zero order parameters of the postshock flows as well with the values inferred for the linear growth rate (the authors compared with our value $u_i^{[5]}$, where five iterations were used for the linear velocity). Also, the linear model used here was compared favorably with the results of the incompressible simulations shown recently in [35]. We will not review those comparisons in more detail here, as a thorough discussion has been presented in the corresponding references and, in general, good agreement with the linear model employed here has been proved in the regimes where linear growth is expected. The authors studied strong shock regimes, where $3 \leqslant M_i \leqslant 10$, with a preshock density ratio in the interval $4 \leqslant R_0 \leqslant 39$ and analyzed the influence of the initial contact surface corrugation amplitude on the late time growth of the instability well into the nonlinear phase. For the cases in which $\psi_0/\lambda \leqslant 0.1$, reasonable agreement between the linear theory results and the simulations was observed.

We turn now our attention to a series of experiments described in [36] and [37].

B. Experiments of [36] and [37]

In [36] the authors have shown experimental data for membrane-free experiments with gases, covering an interesting range of preshock density ratios ($1.817 \leqslant R_0 \leqslant 39$), incident shock Mach numbers from weak to moderately strong shocks, $1.13 \leqslant M_i \leqslant 2.86$, and values of the preshock ripple amplitude/wavelength ratio in the interval $0.01 \leqslant \psi_0/\lambda \leqslant 0.09$, thus providing a formidable data set with which to examine the linear theory, and thus put to rigorous testing the results shown in the previous sections. However, the experiments shown in [37] do actually use a membrane to materialize the interface. Details of the experiments as well as of the diagnostics can be found in Refs. [36,37] and will not be reviewed here. We start with the experiments of [36], studying the growth of their case 5, where a shock comes from N_2 ($\gamma_b = 7/5$) with $M_i \cong 2.86$ and impinges against SF_6 ($\gamma_a = 1.0935$). The preshock density ratio is $R_0 \cong 5.25$, or equivalently, the preshock Atwood number is $A_T \cong 0.68$. The preshock ripple amplitude is $\psi_0 \cong (1.04 \pm 0.09)$ cm and the perturbation wavelength is $\lambda \cong (17.36 \pm 0.27)$ cm, thus giving $\psi_0/\lambda \cong 0.06$. The evolution of the contact surface ripple as a function of time is shown in Fig. 19, where we plot the difference $\psi_i(t) - \psi_0^*$, with ψ_0^* the postshock initial surface corrugation [Eq. (36)]. The purple circles are the experimental data with error bars superposed. The error has been estimated according to the information given in [36]. The solid lines show the temporal evolution following the results of linear theory, as explained in [10] with the solution given as a series of Bessel functions, using Eqs. (34) and (35). Two estimates of the linear asymptotic velocity have been used in the complete solution: curve (a) uses the value $u_i^{[5]}$ with up to five iterations in the functional equation system, curve (b) uses the value $u_i^{[0]}$ given by Eq. (42). We notice that in the time interval during which linear theory is acceptable, we cannot discern between $u_i^{[0]}$ and $u_i^{[5]}$ within the experimental uncertainty. We also show the predictions of different formulations of the impulsive model inside Fig. 19: curve (c) is calculated using the impulsive model prescription $\delta v_{\rm imp}^*$ given by Eq. (52). Curve (d) is calculated with the value $u_{\rm irrot}$ given by Eq. (41), and curve (e) is obtained with the impulsive prescription given

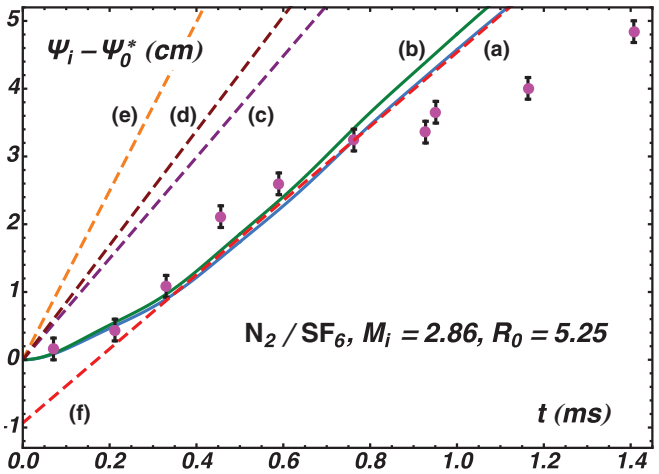

FIG. 19. Comparison between case 5 of [36] and our theoretical model. Curve (a) is calculated with Eq. (35) using $u_i^{[5]}$ in Eq. (34); (b) uses $u_i^{[0]}$; (c) is given by Eq. (52); (d) uses u_{irrot} given by Eq. (41); and (e) uses Eq. (51). The red dashed line (f) is given by Eq. (37).

by Eq. (51). The dotted line superposed on the curve (a) is the asymptotic evolution of the surface ripple predicted by Eq. (37). This dotted line intersects the vertical axis at a value equal to $\psi_\infty - \psi_0^* \cong -0.9328$ cm, which can be calculated with Eqs. (38) and (36). The postshock initial amplitude is, instead, equal to $\psi_0^* \cong 0.53$ cm. This experiment has been also extensively studied by means of numerical simulations in [26], where the important role played by the transmitted shock front has been highlighted. The simulations of [26] followed the ripple growth well beyond the linear phase, identifying important nonlinear features. It is noticed that the reflected shock follows the contact surface in this experiment, as can be seen from Figs. 8 and 9 of [26]. This experiment is analyzed with full details of the linear calculations in Appendix C.

There are some important observations to be made here, concerning Fig. 19. Curves (a) and (b) are obtained with the help of Eq. (34), and follow the linear temporal evolution of the ripple amplitude as a function of time. In order to calculate those curves, not only a significant number of coefficients ω_{2n+1} have to be obtained, but also an accurate estimate of the asymptotic velocity u_i is needed. This velocity has been calculated at first with five iterations ($u_i^{[5]}$) and this value has been used to draw curve (a). A simpler estimate, without iterations [called u_i^0 and given by Eq. (42)], is used inside Eq. (34) to draw curve (b). Both curves are almost indistinguishable within the experimental error inside the interval of time $0+ \leqslant t \lesssim 0.7$ ms, where linear theory is acceptable. The expression given by $u_i^{[0]}$ is the simplest approximation for the model equations used here that consistently takes into account the effect of the bulk vorticities spread inside both fluids. The more accurate value $u_i^{[5]}$ is simply an iteration based on $u_i^{[0]}$ in order to get up to four or more exact digits. The approximate estimate given by $u_i^{[0]}$ should not be confused with the results of previous simpler linear theories based on an impulsive prescription. When compressible effects become important, the formulas based on impulsive models usually give inaccurate results and scalings because they ignore the perturbation dynamics of the shock fronts for $t > 0+$. As they cannot take into account the time variation of the shocks' perturbation pressure, they cannot include the effects of bulk vorticities. The predictions of the impulsive prescriptions have been shown in this work when discussing the very weak shock limit in Sec. V: in Eq. (41) for a double-gravity acceleration impulsive model [11], and in Eqs. (51) and (52) (as initially proposed in [5]). These simpler analytical results are shown here as curves (c), (d), and (e) in Fig. 19, where it is seen that they cannot track the temporal evolution of the contact surface ripple. In fact, impulsive models predict a linear asymptotic ripple growth of the form $\psi_i \cong \psi_0^* + \delta v_{\text{imp}}\, t$, which is different from the asymptotic expression discussed here, and given by Eq. (37): $\psi_i \cong \psi_\infty + \delta v_i^\infty\ t$, which is evidenced as the red dashed line indicated with (f) in that figure. Not only the velocity estimate δv_{imp} is different from δv_i^∞, but also the the postshock ripple amplitude at $t = 0+$, given by ψ_0^*, differs from the exact asymptotic ordinate ψ_∞. Obviously, these differences would tend to zero as we approach the limit of very weak shocks ($M_i - 1 \ll 1$), as already discussed in Sec. V. In fact, from Eq. (39), it is easy to see that $\psi_\infty \sim \psi_0^*$ only if the time integral becomes negligible, which would only happen when $\delta v_i(t) \sim \delta v_i^\infty$ in most of the time integration interval, that is, for extremely weak shocks. Impulsive prescriptions would never predict $\psi_\infty \neq \psi_0^*$, because of the assumption $\delta v_i(t) \sim \delta v_i^\infty\, \mathcal{H}(t)$, with $\mathcal{H}(t) = 1$ if $t > 0+$ and 0 otherwise, $\mathcal{H}$ being the Heaviside function.

We proceed with the other experiments in Fig. 20. In Fig. 20(a) we show the experiments at a lower value of the preshock density ratio $R_0 = 1.817$ where a mix of Ar and He is used as the light gas and pure Ar is the heavier gas. Two scenarios are shown, (1) and (2), which correspond to $M_i = 1.3$ and $M_i = 1.9$, respectively, indicated with a blue square and a red circle. The solid line is the theoretical prediction using the series of Bessel functions and the value $u_i^{[0]}$ has been used, which is indistinguishable from $u_i^{[5]}$ for these experiments, due to the relatively low values of the shock Mach number and low compressibility of the monoatomic gases. As before, the dotted lines represent the asymptotic behavior (in linear theory) of the material surface ripple, according to Eq. (37). These lines intersect the vertical axis at the value ψ_∞ given by Eq. (38). For case 1 we get $\psi_\infty \cong 0.182$ cm, and for case 2 we have $\psi_\infty \cong 0.099$ cm. The postshock surface ripples are, respectively, $\psi_0^* = 0.21$ cm and $\psi_0^* = 0.14$ cm. In Fig. 20(b) we show cases 6, 7, and 8, where a shock comes from He towards SF_6 and the preshock density ratio is $R_0 = 39$. Three Mach numbers are considered as indicated in Fig. 20(b). We plot $\psi_i(t)$ as a function of time, as in Fig. 20(a). The dotted lines are as before, and we have obtained $\psi_\infty = 0.771$ cm for case 6, $\psi_\infty \cong -0.21$ cm for case 7, and $\psi_\infty \cong -0.785$ cm for case 8. We see that the initial transient phase since $t = 0+$ is well described using the series of Bessel functions, until nonlinearity becomes dominant and the data continue growing with a different law. In Fig. 21 we show the analog of Fig. 4 in which we plot $k[\psi_i(t) - \psi_\infty]$ as a function of $k\delta v_i^\infty t$, to stress the fact that all the curves should asymptotically collapse into a single line of slope 45°, within the limit of validity of linear theory. We use $\delta v_i^\infty = k\psi_0 D_i u_i^{[0]}$. It is evident that each experiment has a small window of linear evolution which depends on the value of ψ_0/λ. The smaller

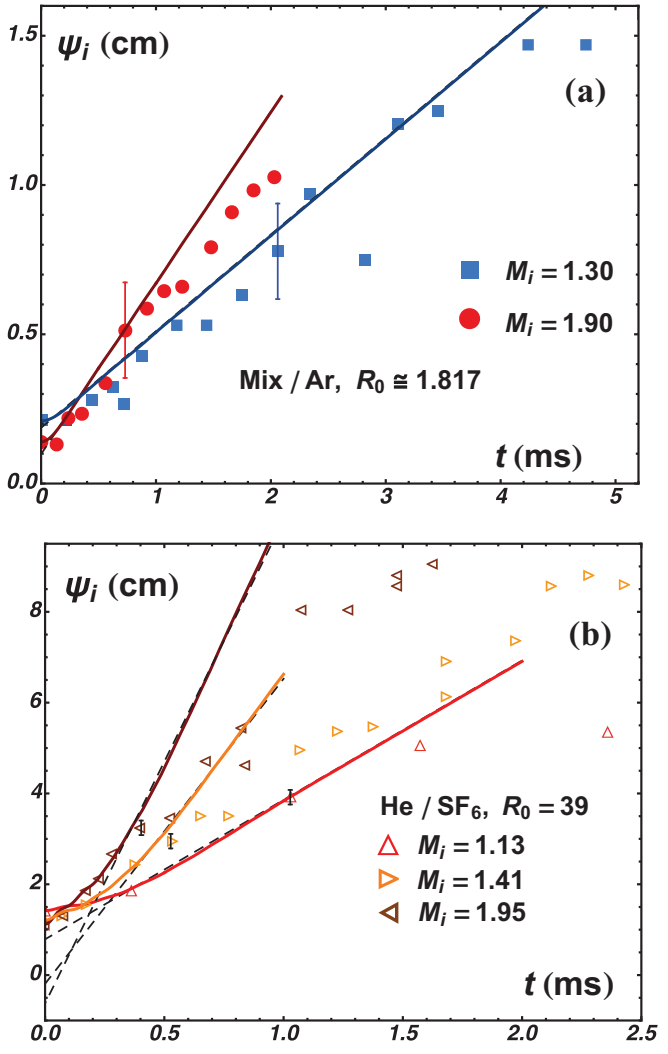

FIG. 20. (a) Temporal evolution of the contact surface ripple for cases 1 and 2 of [36]. The solid lines are calculated with Eq. (35) using $u_i^{[0]}$ in Eq. (34). The dashed lines are given by Eq. (37). (b) Same as (a) for cases 6, 7, and 8 of [36].

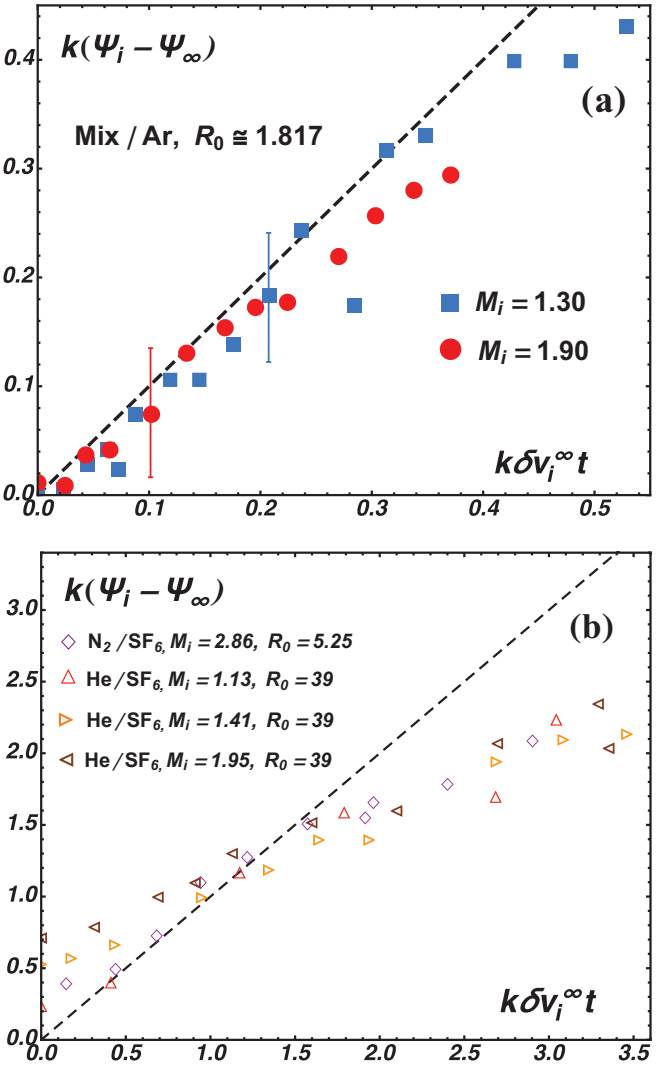

FIG. 21. (a) Plot of $k[\psi_i(t) - \psi_\infty]$ as a function of $k\delta v_i^\infty t$ for case 1 of [36]. (b) Same as (a) for cases 5, 6, 7, and 8 of [36]. The dashed line represents the asymptotic behavior predicted by Eq. (37).

this ratio, the longer will last the linear behavior predicted by Fig. 4. In Fig. 21, each experiment leaves the linear asymptotic scaling at a different time, strongly dependent on the value of ψ_0/λ as discussed in [23–27], marking the beginning of nonlinear growth. We notice in Fig. 21(b) that their case 5 follows the asymptotic law Eq. (37) inside the dimensionless time interval $0.4 \leqslant k\delta v_i^\infty t \leqslant 1.6$. Case 6 shows the similar trend inside the interval $0.4 \leqslant k\delta v_i^\infty t \leqslant 1.7$. Cases 7 and 8 show a smaller interval of agreement with Eq. (37). Finally, we show in Fig. 22 the comparison with the experiments of [37], where the gases are air and SF_6. They showed two experiments with the same preshock density ratio ($R_0 \cong 5.23$), or equivalently an Atwood number $A_T \cong 0.679$, and an incident shock Mach number ($M_i \cong 1.45$). The wavelength is $\lambda = 8$ cm and two different values for ψ_0: 0.306 cm and 0.918 cm. The ψ_0/λ values are 0.027 and 0.083, respectively. The second experiment with larger initial amplitude is therefore marginally nonlinear. The plot shows $k\psi_i(t) - k\psi_\infty$ as a function of the dimensionless time $k\delta v_i^\infty t$. The time window

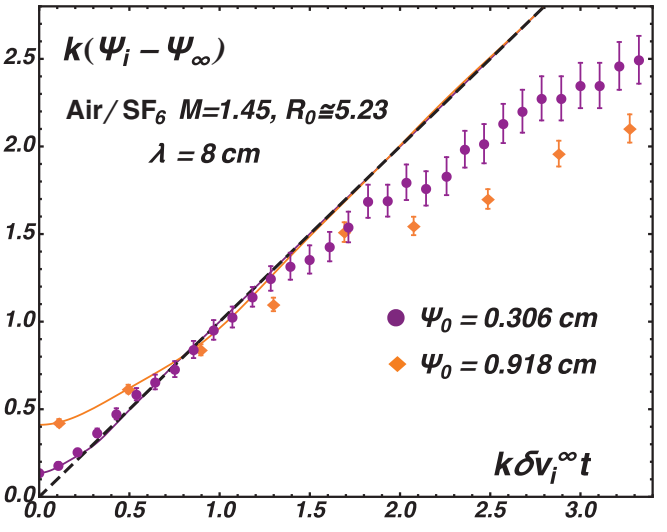

FIG. 22. Plot of $k[\psi_i(t) - \psi_\infty]$ as a function of $k\delta v_i^\infty t$ for cases 1 and 2 of [37]. The solid lines are calculated with Eq. (35) using $u_i^{[0]}$.

TABLE I. Description of the preshock parameters used in the experiments of [36,37]. The last two columns refer to the values of the asymptotic ordinate of the contact surface ripple [Eq. (38)] and the asymptotic linear normal velocity predicted. These two quantities are calculated using five iterations in the corresponding functional equation.

Case/Ref.[ ]	γ_a	γ_b	R_0	M_i	ψ_0(cm)/λ(cm)	ψ_∞ (cm)	δv_i^∞ (m/s)
1[36]	5/3	5/3	1.817	1.30	0.29/20.15	0.187	3.24
2[36]	5/3	5/3	1.817	1.90	0.26/17.92	0.098	5.47
5[36]	1.0935	7/5	5.25	2.86	1.04/17.36	−0.389	55.48
6[36]	1.0935	5/3	39	1.13	1.50/16.94	0.777	30.70
7[36]	1.0935	5/3	39	1.41	1.38/16.74	−0.192	66.75
8[36]	1.0935	5/3	39	1.95	1.36/16.70	−0.771	100.43
1[37]	1.0935	7/5	5.23	1.45	0.306/8	0.045	13.65
2[37]	1.0935	7/5	5.23	1.45	0.918/8	0.134	50.40

over which the data follow the asymptotic linear scaling is given by $0.2 \leqslant k\delta v_i^\infty t \leqslant 1.4$ for the case with smaller initial amplitude. In Table I we give information on the experiments of [36] studied here, as well as the experiments of [37]. We indicate the preshock parameters and also the values inferred for the asymptotic ripple ordinate (ψ_∞) together with the asymptotic normal velocity (δv_i^∞) values that were used to plot the temporal evolution, according to Eqs. (34)–(38). The asymptotic ordinate and material velocity have been calculated with five iterations. In Table II we show the values obtained for the dimensionless normal velocity (u_i), calculated using the different approximations discussed in the preceding sections. Blank spaces in Table II are left because the preshock parameters do not fulfill the constraints required in the corresponding equation referred to in the first column.

VII. SUMMARY

In the present work we have shown analytical expressions for the asymptotic velocities that develop at a shocked contact surface when another shock is reflected. The analytical model used solves exactly the fluid equations in the linear regime for the perturbations generated between the rippled transmitted and reflected wave fronts. Initial generation of transverse velocities at the contact surface is the main cause of the subsequent evolution of the perturbation dynamics. Even though the equation of state used here is that of an ideal gas for both fluids, the results of the model are not restricted by this assumption and more complex equations of state can be studied. The critical parameter governing vorticity, entropy, and sound perturbation generation behind each shock front is the slope of the Rankine-Hugoniot curve. Therefore, knowing the dependence of this quantity on the preshock parameters would allow us to study the RMI in other EOS fluids. In the cases considered here, ideal gases described by their isentropic exponents have been taken into account. For situations where compression is important, the vorticity field created by the shocks is an important quantity in order to accurately determine the steady state asymptotic velocity that characterizes the asymptotic RMI. Unfortunately, the involved mathematics is complicated because of the coupling between the reflected and transmitted shocks, which obliges us to iterate over a coupled functional equation in order to obtain information until the asymptotic phase is reached. The equations can be solved to follow the amplitude of the material surface ripple in time and good agreement is observed for the initial transient phase and during the interval of time when the asymptotic linear growth is expected. The initial transient phase can be neatly followed and agreement with experiments is very good. This agreement is better for those experiments with $\psi_0/\lambda \lesssim 0.1$. As an additional result, the scaling $\psi_i(t) \sim \psi_\infty + \delta v_i^\infty\, t$ has been found, where ψ_∞ is, in general, quite different from the postshock ripple amplitude at $t = 0+$, another important effect of compressibility. The ordinate ψ_∞ can be measured in recent experiments. As for the asymptotic ripple velocities, a general formula can be obtained by iterating a finite number of times. It is seen that in all the cases that can be studied in experiments and simulations, the asymptotic linear normal velocity is proportional to the incident shock velocity. If we define, for example, a characteristic velocity $v_c = \sqrt{p_0/\rho_{b0}}$, we can conclude that $\delta v_i/(k\psi_0 v_c) = f(\gamma_a, \gamma_b, R_0, M_i)M_i$. For very strong shocks, f is independent of M_i, as in [39], making $\delta v_i \propto D_i$ in this limit. The function f generally depends on the four preshock parameters γ_a, γ_b, R_0,

TABLE II. Estimations of the linear asymptotic normal velocity of the experiments discussed, using the different formulas presented in the work.

Growth rate Case/Ref.[ ]	1[36]	2[36]	5[36]	6[36]	7[36]	8[36]	1/2[37]
Eq. (40) ($u_i^{[5]}$)	0.0626	0.0847	0.1463	0.0470	0.0876	0.0976	0.1599
Eq. (42) ($u_i^{[0]}$)	0.0626	0.0847	0.1521	0.0470	0.0882	0.1036	0.1619
Eq. (45) ($M_i - 1 \ll 1$)	0.0617			0.0516			0.2681
Eq. (55) ($M_i \gg 1$)		0.1021	0.1713		0.0851	0.1000	0.2373
Eq. (56) ($R_0 - R_0^m \ll 1$)	0.0572	0.0787					
Eq. (57) ($R_0 \gg 1$)				0.0467	0.0878	0.1028	0.0963

and M_i and is the quantity that has been one the objectives of our calculations in this work. Several approximate expressions to f have been compared with the exact solution in different regimes. Assuming a completely irrotational velocity field in each compressed fluid turns out to be a good approximation only for incident shock Mach numbers $M_i \lesssim 1.3$. At higher compressions the disagreement might become quite important depending on the fluid compressibility and on the preshock density ratio. An approximate formula is proposed, named here $u_i^{[0]}$, and written in Eq. (42). It is obtained after an initial guess of the pressure functions is done when iterating on the functional equation. The agreement between this expression and the exact value is shown in different situations with varying degrees of compression. Despite its apparent algebraic complexity, it is the simplest expression that can be obtained from the linear theory up to date which consistently takes into account the rotational character of the velocity fields generated by the corrugated shocks. The agreement between the exact solution and the approximate one is studied as a function of the incident shock Mach number. Besides, the behavior of the tangential velocities v_{ia}, v_{ib} and the vorticity parameters (F_a and F_b) has also been briefly discussed. We conclude that the assumption of an irrotational velocity field [characterized with the irrotational estimate of the normal velocity u_{irrot} given by Eq. (41)] is not a very good hypothesis over wide regions of the space of preshock parameters and when compression is important, we conclude in general that $u_i < u_{\text{irrot}}$. Nevertheless, we have found small regions of the preshock parameter space, not surprisingly near to freeze-out conditions, in which the exact growth rate u_i is actually larger than the irrotational estimation u_{irrot}. This unexpected result deserves attention and will be studied in the future. Motivated by all these results, a different set of approximate expressions, based on Taylor expansions of a small parameter, have been presented, each one valid in a different physical limit, following the same strategies as in [39]. At first, the weak shock regime is analyzed by expanding the quantities that compose the normal velocity in powers of $M_i - 1$. The first term of the expansion confirms the validity of the impulsive approximation of Richtmyer for $M_i - 1 \lesssim 1.1$. A reformulation of the impulsive model (presented in [10]) that exactly agrees with u_{irrot} is shown to be valid up to $M_i \lesssim 1.2$. In order to include bulk vorticity effects, we expanded the normal velocity up to the fourth power in $M_i - 1$. We have found that adding more terms is not practical because the convergence of the series is generally limited to $M_i \lesssim 1.3$. Using the expression for $u_i^{[0]}$, we can calculate the growth rate in most of the parameter space with small error, except perhaps, when compressibility is very demanding. Taylor expansions of $u_i^{[0]}$ in powers of $1/M_i$, $R_0 - R_0^m$, and $1/R_0$ have been presented and compared with the exact solution. Contrary to the results shown in [39], the results obtained here show more complicated mathematical formulas. This is a very unpleasant feature of the calculations for RMI with two fluids. The reason underlying such complexity resides in the very nature of the functional equations that describe the interaction of both shocks. Any time one of the rippled shocks oscillates, it generates velocity and pressure perturbations that are felt some finite time later on the other rippled shock which in turn reacts and so on. The process repeats indefinitely, giving rise to a complicated pattern of reverberations which couple the velocity fields in each fluid. Weak shocks travel very fast in comparison to the compressed material surface, and therefore just an irrotational velocity field is enough to deal with the asymptotic perturbed motion. When compression becomes important, at least the transmitted shock moves very slowly relative to the compressed contact surface, and this fact enhances coupling through reverberation, complicating the underlying calculations. Nevertheless, good agreement has been demonstrated with recent experiments in a wide range of preshock density ratios, fluid compressibilities, and incident shock strengths, in which not only the different asymptotic expressions obtained here have compared favorably with the measured data, but also the temporal evolution of the transient phase fits accurately. The main signature of the compression by rippled shocks of ideal gases is the generation of vorticity in the bulk. This vorticity has also been identified in recent simulations and is an important ingredient to be taken into account if more accurate nonlinear models are to be developed. Besides, the scaling of the kinetic energy contained in the more intense vortices near the contact surface is still an interesting and open question.

ACKNOWLEDGMENTS

The authors would like to thank A. R. Piriz and A. Bret (UCLM) for encouragement and support. C. Huete (Universidad Carlos III, Madrid) is acknowledged for helpful comments and for providing assistance with the figures. F.C.C. acknowledges support from UCLM for a predoctoral fellowship. This work has received support from MINECO under Grant No. ENE2013-45661-C2-1-P and from JCCM, PEI-2014-008.

APPENDIX A: FUNCTIONAL EQUATIONS

In this section, we show the functional equations satisfied by the pressure amplitudes F_{m1} and F_{m2} in order to calculate the pressure perturbations in both fluids. As discussed in [15], we have the following relationships:

$$\begin{aligned} F_{a2}(q_a) &= \frac{\sinh\chi_t\ \tilde{v}_{ya}^0}{\sinh(q_a-\chi_t)\eta_t^+(q_a-\chi_t)} \\ &\quad -\frac{\eta_t^-(q_a-\chi_t)}{\eta_t^+(q_a-\chi_t)}F_{a1}(q_a-2\chi_t), \\ F_{b1}(q_b) &= \frac{\sinh\chi_r\ \tilde{v}_{yb}^0}{\sinh(q_b+\chi_r)\eta_r^-(q_b-\chi_r)} \\ &\quad -\frac{\eta_r^+(q_b+\chi_r)}{\eta_r^-(q_b-\chi_r)}F_{b2}(q_b+2\chi_r), \end{aligned} \tag{A1}$$

with the functions $\eta_{r,t}^{\pm}$ defined as

$$\eta_r^{\pm}(q_b) = \frac{\alpha_{b1}(q_b)}{\cosh q_b} \pm 1, \quad \eta_t^{\pm}(q_a) = \frac{\alpha_{a1}(q_a)}{\cosh q_a} \pm 1 \tag{A2}$$

and

$$\alpha_{m1}(q_m) = \alpha_{m10}\sinh q_m + \frac{\alpha_{m11}}{\sinh q_m},\ \alpha_{m2}(q_m) = \frac{\alpha_{m20}}{\sinh q_m}. \tag{A3}$$

The values of α_{m10}, α_{m11}, and α_{m20} are

$$\begin{aligned}
\alpha_{b10} &= \frac{M_r^2+1}{2M_r\beta_r},\ \alpha_{b11} = -\frac{1}{2\beta_r},\ \alpha_{b20} = -\tilde{v}_{yb}^0\sinh\chi_r,\\
\alpha_{a10} &= \frac{M_t^2+1}{2M_t\beta_t},\ \alpha_{a11} = -\frac{1}{2\beta_t},\ \alpha_{a20} = -\tilde{v}_{ya}^0\sinh\chi_t.
\end{aligned} \tag{A4}$$

After some additional algebraic manipulations, which are explained in previous works, we obtain a coupled system of functional equations [15]:

$$\begin{aligned}
\phi_{a3}(q_a)F_{a1}(q_a) + F_{b2}(q_b) &= \phi_{a1}(q_a) + \phi_{a2}(q_a)F_{a1}(q_a - 2\chi_t),\\
F_{a1}(q_a) + \phi_{b3}(q_b)F_{b2}(q_b) &= \phi_{b1}(q_b) + \phi_{b2}(q_b)F_{b2}(q_b + 2\chi_r).
\end{aligned} \tag{A5}$$

The functions ϕ_{mj}:

$$\begin{aligned}
\phi_{a1}(q_a) &= \frac{\Delta+1}{2}\frac{\sinh\chi_t\ \tilde{v}_{ya}^0}{\sinh(q_a-\chi_t)\eta_t^+(q_a-\chi_t)},\quad \phi_{b1}(q_b) = \frac{\Delta+1}{2\Delta}\frac{\sinh\chi_r\ \tilde{v}_{yb}^0}{\sinh(q_b+\chi_r)\eta_r^-(q_b+\chi_r)},\\
\phi_{a2}(q_a) &= -\frac{\Delta+1}{2}\frac{\eta_t^-(q_a-\chi_t)}{\eta_t^+(q_a-\chi_t)},\quad \phi_{b2}(q_b) = -\frac{\Delta+1}{2\Delta}\frac{\eta_r^+(q_b+\chi_r)}{\eta_r^-(q_b+\chi_r)},\\
\phi_{a3}(q_a) &= \frac{1-\Delta}{2},\quad \phi_{b3}(q_b) = \frac{\Delta-1}{2\Delta},
\end{aligned} \tag{A6}$$

where $\Delta = R\cosh q_b/\cosh q_a$. The above system of equations allows us to find F_{a1}, F_{b2} by iterations (and hence $\tilde{P}$ and $\tilde{H}$). This is done as in [39], by considering the simplest solution to the coupled system of functional relationships given in Eqs. (A5). It amounts to neglecting the arguments $-2\chi_t$ and $2\chi_r$ in the functions F_{a1} and F_{b2}. This is equivalent to considering Eqs. (A5) as a much simpler algebraic set of two equations in two unknowns: $F_{a1}(q_a)$ and $F_{b2}(q_b)$. Using this approximation, we get a first estimate, which we call $F_{a1}^{[0]}$ and $F_{b2}^{[0]}$:

$$\begin{aligned}
F_{b2}^{[0]}(q_b) &\cong \frac{\phi_{a1}(q_a) - \phi_{b1}(q_b)[\phi_{a3}(q_a) - \phi_{a2}(q_a)]}{1 - [\phi_{b3}(q_b) - \phi_b(q_{b2})][\phi_{a3}(q_a) - \phi_{a2}(q_a)]},\\
F_{a1}^{[0]}(q_a) &\cong \phi_{b1}(q_b) - \phi_{b3}(q_b)F_{b2}^{[0]}(q_b) + \phi_{b2}(q_b)F_{b2}^{[0]}(q_b + 2\chi_r).
\end{aligned} \tag{A7}$$

We recall that the variables q_a and q_b are related by $N\sinh q_a = \sinh q_b$, where $N = c_{af}/c_{bf}$. Once we compute the initial functions $F_{a1}^{[0]}$ and $F_{b2}^{[0]}$ we can continue with the procedure and obtain new functions $F_{a1}^{[1]}$ and $F_{b2}^{[1]}$ in a second iteration round, using the functions $F_{a1}^{[0]}$ and $F_{b2}^{[0]}$ on the right hand sides of Eqs. (A5). Proceeding further we can define a sequence of functions $F_{a1}^{[n]}$ and $F_{b2}^{[n]}$, where all of them would be nested around the initial set $F_{a1}^{[0]}$ and $F_{b2}^{[0]}$. It is observed that the iteration procedure nested around $F_{a1}^{[0]}(q_a)$ and $F_{b2}^{[0]}(q_b)$ given in Eq. (A7) is reasonably accurate for relatively large values of q_a and q_b, which is all we need to compute the dimensionless asymptotic velocity u_i. However, if we wanted to calculate ψ_∞ [as given by Eq. (38)], we would need the first derivatives of the functions F_{b1} and F_{b2} evaluated at $q_b = 0$. Therefore, the approximation used in this appendix is not convenient and another approach is necessary to get accurate values of the pressure amplitudes at $q_a = q_b = 0$. This point is touched on later in Appendix C.

APPENDIX B: ASYMPTOTIC VELOCITY PROFILES IN BOTH FLUIDS

We write in this appendix the differential equations satisfied by the asymptotic velocity fields, when the corrugated shocks are very far from the material interface. We then derive the boundary conditions imposed on the asymptotic velocities at both sides of the contact surface, to warrant boundedness of the perturbations in the whole space.

It is not difficult to see that $\vec{\tilde{v}}_{rot}$, defined in Eq. (28), is a solenoidal field; that is, the perturbations u and v in the last equation determine an incompressible velocity field. Therefore, they satisfy

$$\frac{du}{dx} + v = 0. \tag{B1}$$

We need another equation to connect u and v which is constructed paying attention to the rotational character of the velocity field, through the generation of vorticity behind each corrugated shock. As vorticity is a conserved quantity on each fluid element, its value comes from the vorticity that the fluid element picked behind the shock front position, at the time the shock front

compressed that fluid particle. In our problem, the dimensionless z component of vorticity is

$$\tilde{\omega}(x,y) = \frac{\delta\omega}{kD_i} = g(\tilde{x})\sin\tilde{y}. \tag{B2}$$

Following [15,29,32], we have the vorticity functions g_a and g_b, in each fluid, respectively:

$$\begin{aligned} g_a(\tilde{x}) &= \Omega_a \tilde{p}_t(r_t = \tilde{x}/|\sinh\chi_t|), \\ g_b(\tilde{x}) &= \Omega_b \tilde{p}_r(r_r = \tilde{x}/\sinh\chi_r). \end{aligned} \tag{B3}$$

The quantities $\Omega_{a,b}$ are [15,29,32]

$$\begin{aligned} \Omega_a &= -\frac{\left(M_t^2-1\right)\sqrt{2\gamma_a M_t^2-\gamma_a+1}}{M_t^2\left[(\gamma_a-1)M_t^2+2\right]^{3/2}}, \\ \Omega_b &= \frac{\left(M_r^2-1\right)^2\sqrt{2\gamma_b M_r^2-\gamma_b+1}}{M_r^2\left[(\gamma_b-1)M_r^2+2\right]^{3/2}}. \end{aligned} \tag{B4}$$

Therefore, the additional differential equation satisfied by the normal and tangential components of the velocity is

$$\frac{dv}{dx} + u = g(x). \tag{B5}$$

Combining Eqs. (B1) and (B5), the equations satisfied by the x and y components of the rotational velocity fields in both fluids are

$$\begin{aligned} \frac{d^2u_a}{d\tilde{x}^2} - u_a &= -g_a, \quad \frac{d^2v_a}{d\tilde{x}^2} - v_a = \frac{dg_a}{d\tilde{x}}, \\ \frac{d^2u_b}{d\tilde{x}^2} - u_b &= -g_b, \quad \frac{d^2v_b}{d\tilde{x}^2} - v_b = \frac{dg_b}{d\tilde{x}}. \end{aligned} \tag{B6}$$

We can Laplace-transform both equations integrating in the variable $|x|$, as in [15,29,32]. We define the functions

$$U_m(\sigma_m) = \int_0^\infty u_m(\tilde{x})\exp(-\sigma_m|\tilde{x}|)d\tilde{x}. \tag{B7}$$

We multiply by $\exp(-\sigma_m|\tilde{x}|)$ both sides of both Eqs. (B6) and integrate in the whole space at each fluid to obtain

$$\begin{aligned} U_a(\sigma_a) &= \frac{-\sigma_a|u_i| + |v_{ia}| - \Omega_a\sinh\chi_t\tilde{P}_t(-\sigma_a\sinh\chi_t)}{\sigma_a^2-1}, \\ U_b(\sigma_b) &= \frac{\sigma_b|u_i| - |v_{ib}| - \Omega_b\sinh\chi_r\tilde{P}_r(\sigma_b\sinh\chi_r)}{\sigma_b^2-1}, \end{aligned} \tag{B8}$$

where u_i is the asymptotic normal velocity at the contact surface and v_{ia} and v_{ib} are the asymptotic tangential velocities at both sides. The functions $\tilde{P}_t$ and $\tilde{P}_r$ are understood as functions of the corresponding variable q. It is clear that u_a and u_b are bounded functions in the whole space. Therefore, their spatial Laplace transforms exist for any real value of their arguments σ_a and σ_b, respectively, and therefore, there should be no singularity for $\sigma_a = \sigma_b = 1$. Therefore, we must require, as done in [39],

$$\begin{aligned} |u_i| - |v_{ia}| &= -\Omega_a\sinh\chi_t\tilde{P}_t(q_a = -\chi_t) = F_a, \\ |u_i| - |v_{ib}| &= \Omega_b\sinh\chi_r\tilde{P}_r(q_b = \chi_r) = -F_b, \end{aligned} \tag{B9}$$

where F_m is the dimensionless form of $\mathcal{F}_m$ [see Eqs. (2)]. To calculate them, we use the values of $F_{a1}(-2\chi_t)$ and $F_{b2}(2\chi_r)$ with the expressions obtained in Appendix A.

APPENDIX C: CALCULATION OF ψ_∞

We recall here the definition of the asymptotic ordinate ψ_∞:

$$\psi_\infty = \psi_0^* - \frac{D_i}{c_{bf}}[F_{b1}'(0) - F_{b2}'(0)]\psi_0, \tag{C1}$$

where we realize the need to calculate the derivatives of F_{b1} and F_{b_2} at the origin $q_b = 0$. This last fact suggests that we consider Eqs. (A5) in the limit $|q_{a,b}| \ll 1$. To this scope we approximate, by making first order Taylor expansions at the

origin:

$$F_{a1}(q_a - 2\chi_t) \cong F_{a1}(-2\chi_t) + q_a F'_{a1}(-2\chi_t) + O[(q_a)^2],$$
$$F_{b2}(q_b + 2\chi_r) \cong F_{b2}(2\chi_r) + q_b F'_{b2}(2\chi_r) + O[(q_b)^2]. \quad \text{(C2)}$$

If we substitute inside Eq. (A5), we obtain, for $q_a \ll -\chi_t$ and $q_b \ll \chi_r$,

$$F_{a1}(q_a) \cong \frac{\phi_{a1}(q_a)\phi_{b3}(q_b) - \phi_{b1}(q_b)}{\phi_{a3}(q_a)\phi_{b3}(q_a) - 1} + \frac{\phi_{a2}(q_a)\phi_{b3}(q_b)}{\phi_{a3}(q_a)\phi_{b3}(q_b) - 1} F_{a1}(-2\chi_t) - \frac{\phi_{b2}(q_b)}{\phi_{a3}(q_a)\phi_{b3}(q_b) - 1} F_{b2}(2\chi_r)$$
$$+ \frac{q_a\phi_{a2}(q_a)\phi_{b3}(q_b)}{\phi_{a3}(q_a)\phi_{b3}(q_b) - 1} F'_{a1}(-2\chi_t) - \frac{q_b\phi_{b2}(q_b)}{\phi_{a3}(q_a)\phi_{b3}(q_b) - 1} F'_{b2}(2\chi_r),$$

$$F_{b2}(q_b) \cong \frac{\phi_{b1}(q_b)\phi_{a3}(q_a) - \phi_{a1}(q_a)}{\phi_{a3}(q_a)\phi_{b3}(q_b) - 1} - \frac{\phi_{a2}(q_a)}{\phi_{a3}(q_a)\phi_{b3}(q_b) - 1} F_{a1}(-2\chi_t) + \frac{\phi_{a3}(q_a)\phi_{b2}(q_b)}{\phi_{a3}(q_a)\phi_{b3}(q_b) - 1} F_{b2}(2\chi_r)$$
$$- \frac{q_a\phi_{a2}(q_a)}{\phi_{a3}(q_a)\phi_{b3}(q_b) - 1} F'_{a1}(-2\chi_t) + \frac{q_b\phi_{a3}(q_a)\phi_{b2}(q_b)}{\phi_{a3}(q_a)\phi_{b3}(q_b) - 1} F'_{b2}(2\chi_r). \quad \text{(C3)}$$

The function $F_{b1}(q_b)$ can be obtained from the linearized Rankine-Hugoniot equations summarized in Eq. (A1). We repeat it here for completeness, after substituting the approximate expression for $F_{b2}(q_b + 2\chi_r)$, as given by Eq. (C2) before:

$$F_{b1}(q_b) \cong \frac{\sinh\chi_r\ \tilde{v}^0_{yb}}{\sinh(q_b + \chi_r)\eta_r^-(q_b - \chi_r)} - \frac{\eta_r^+(q_b + \chi_r)}{\eta_r^-(q_b - \chi_r)} F_{b2}(2\chi_r) - \frac{q_b\ \eta_r^+(q_b + \chi_r)}{\eta_r^-(q_b - \chi_r)} F'_{b2}(2\chi_r). \quad \text{(C4)}$$

We see that the values of the pressure amplitudes F_{a1}, F_{b2} (and of their derivatives) at $q_a = q_b = 0$ depend on the values at $q_a = -2\chi_t$ and $q_b = 2\chi_r$. This is due to the functional character of Eqs. (A5), related to the acoustic reverberations that occur in the space between both fronts. Therefore, the accuracy with which we can calculate ψ_∞ is dependent on the accuracy with which we calculate the quantities $F_{a1}(-2\chi_t)$, $F_{b2}(2\chi_r)$, $F'_{a1}(-2\chi_t)$, and $F'_{b2}(2\chi_r)$. These last quantities can be calculated with the expressions derived in Appendix A above, using the expressions derived for large values of the arguments $q_a \geqslant -\chi_t$ and $q_b \geqslant \chi_r$. The number of iterations necessary to calculate them with a given number of digits will be a function of the four preshock parameters. For weak shocks, in general, just the seed values used, without iterations, are usually enough. For moderate to strong shocks, one or two iteration rounds may be necessary, until the wanted number of significant/accurate digits is obtained.

APPENDIX D: DETAILED CALCULATIONS FOR CASE 5 OF [36]

1. Zero order quantities

We show here the different algebraic steps to calculate the temporal evolution and the linear asymptotic velocity for one of the experiments discussed before. We consider case 5 of [36], discussed at the beginning of Sec. VI. A shock comes from air ($\gamma_b = 7/5$) towards SF_6 ($\gamma_a = 1.0935$). The value chosen for γ_a has been taken from [8]. The preshock density ratio is $R_0 = 5.25$, which gives a preshock Atwood number $A_T = 0.68$. The preshock ripple amplitude is $\psi_0 = 1.04$ cm and the corrugation wavelength is $\lambda = 17.36$ cm. The incident Mach number is $M_i = 2.86$. Therefore, the incident shock strength is $z_i = 2\gamma_b(M_i^2 - 1)/(\gamma_b + 1) \cong 8.376200$. The initial sound speeds are $c_{a0} = 13.4882$ cm/ms for SF_6, and $c_{b0} = 34.9693$ cm/ms for air. Therefore, the ratio of preshock sound speeds is $c_{a0}/c_{b0} \cong 0.385714$. The incident shock speed is $D_i = -100.012$ cm/ms. The reflected and transmitted shock strengths, according to the solution of Eqs. (9) and (10), are $z_r \cong 0.801833$ and $z_t \cong 15.894346$. The upstream reflected and transmitted Mach numbers are, according to Eqs. (6), $M_r \cong 1.298955$ and $M_t \cong 4.026763$. The corresponding downstream Mach numbers are, respectively, $\beta_r \cong 0.786488$ and $\beta_t \cong 0.315299$. We display below the different ratios of postshock quantities. We show first the ratios behind the incident front, according to Eq. (4):

$$\frac{\rho_{b1}}{\rho_{b0}} \cong 3.723755, \quad \frac{c_{b1}}{c_{b0}} \cong 1.586803, \quad \frac{U_1}{c_{b0}} \cong -2.091958. \quad \text{(D1)}$$

For this experiment, we thus have $c_{b1} \cong 55.4895$ cm/ms and $U_1 \cong -73.1544$ cm/ms. The negative sign for U_1 simply indicates that the fluid behind the incident shock moves from right to left (see Fig. 1).

We also calculate the ratios across the reflected and transmitted shocks, using the expressions inside Eq. (7):

$$\frac{\rho_{bf}}{\rho_{b1}} \cong 1.513875, \quad \frac{\rho_{af}}{\rho_{a0}} \cong 9.654408,$$
$$\frac{c_{bf}}{c_{b1}} \cong 1.090969, \quad \frac{c_{af}}{c_{a0}} \cong 1.322842,$$
$$\frac{U_1 - U}{c_{b1}} \cong 0.4409218, \quad \frac{U}{c_{a0}} \cong 3.609672. \quad \text{(D2)}$$

The ratio of final densities and final sound velocities, at the contact surface, are

$$R = \frac{\rho_{af}}{\rho_{bf}} \cong 8.991123, \quad N = \frac{c_{af}}{c_{bf}} \cong 0.294740. \quad \text{(D3)}$$

We thus have the results $c_{af} = 17.842753$ cm/ms and $c_{bf} = 66.205234$ cm/ms. In the laboratory frame, we have $U = -48.687983$ cm/ms, $D_r \cong -1.076082$ cm/ms, and $D_t = -54.313785$ cm/ms. We see that the reflected shock moves following the contact surface.

For this choice of gases and incident Mach number, the preshock density ratio for which no shock would be reflected is, according to Eq. (11), $R_0^m \cong 1.161252$, which is far from the preshock density ratio used in this experiment.

2. First order quantities

We show here the values of the perturbed quantities, relevant for the calculation of the final velocities. The initial corrugations of the transmitted and reflected shocks, in units of ψ_0, are given as functions of the velocity ratios, D_t/D_i and D_r/D_i, which have to be calculated from Eqs. (D1) and (D2):

$$\begin{aligned}\frac{\psi_{t0}}{\psi_0} &= 1-\frac{D_t}{D_i} = 1-\frac{D_t}{c_{a0}}\frac{c_{a0}}{c_{b0}}\frac{c_{b0}}{D_i} \cong 0.456930,\\ \frac{\psi_{r0}}{\psi_0} &= 1+\frac{D_r}{D_i} = 1+\frac{D_r+U_1}{c_{b1}}\frac{c_{b1}}{c_{b0}}\frac{c_{b0}}{D_i}-\frac{U_1}{c_{b0}}\frac{c_{b0}}{D_i}\\ &\cong 0.989240 < 1. \end{aligned} \tag{D4}$$

We see a curious result in Eq. (D4) above: the initial corrugation of the reflected shock is less than the initial contact surface ripple amplitude. This is a particular case in which the reflected shock follows the compressed contact surface, because $D_r < 0$ in the laboratory frame. Therefore, as a result of the refraction of the incident shock, all three surfaces—the transmitted shock, the contact surface, and the reflected shock—move to the left in Fig. 1. This possibility has been highlighted in [43]. This result can also be seen in Figs. 8 and 9 of [26]. For example, at $t = 0.25$ ms, the reflected shock position is $x_r \sim 100.5$ cm and at $t = 0.50$ ms it is $x_r \sim 100.08$ cm. Therefore, their reflected shock moved very little from left to right, in the laboratory frame, following the contact surface, with an approximate speed of $|D_r| \sim 1.2$ cm/ms (their positive $\hat{x}$ axis points opposed to ours). The value obtained from the simulation pictures compares reasonably well with our estimate: $D_r \sim -1.08$ cm/ms, and with the value deduced from the experiments. The relative difference between linear theory and experiments, on one hand, and simulations in this case for the reflected shock velocity remains within 10%. It is clear from the simulation snapshots that the reflected front follows the material surface.

This possibility opens the road for additional interesting questions, such as, would it be possible to have reflected shock fronts following the contact surface with large enough values of $|D_r|$ such that $\psi_{r0} < 0$? Probably, for sufficiently strong shocks, this possibility should not be ruled out. This observation connects with the discussion done in Sec. V about freeze-out for strong shocks in the shock reflected case. If $\psi_{r0} < 0$, the sign of δv^0_{yb} also changes, thus making $\delta v^0_{ya}/\delta v^0_{yb} > 0$, which has been found a necessary condition for freeze-out [17,44]. As these situations are quite speculative at the moment, and far beyond the scope of the present paper, they will be considered in a future work.

For the experiment under discussion, the initial tangential velocities, behind the transmitted and reflected shocks in units of $k\psi_0 D_i$, are, according to Eq. (16),

$$\begin{aligned}\tilde{v}^0_{ya} &= \frac{\delta v^0_{ya}}{k\psi_0 D_i} = -\frac{U}{D_i}\left(1-\frac{D_t}{D_i}\right) \cong -0.222442,\\ \tilde{v}^0_{yb} &= \frac{\delta v^0_{yb}}{k\psi_0 D_i} = \frac{U_1-U}{D_i}\left(1+\frac{D_r}{D_i}\right) \cong 0.242003. \end{aligned} \tag{D5}$$

The negative sign for $\tilde{v}^0_{ya}$ indicates that it is opposed to $\tilde{v}^0_{yb}$. The values of the real velocities achieved in this experiment, in dimensional units, are

$$\delta v^0_{ya} \cong -8.373997 \text{ cm/s}, \quad \delta \mathrm{v}^0_{\mathrm{yb}} \cong 9.1103677 \text{ cm/s}. \tag{D6}$$

With the postshock quantities obtained before, we can calculate the temporal evolution of the pressure perturbations with the aim of describing the contact surface ripple growth together with the calculation of the asymptotic normal and tangential velocities in the linear phase. Using the algebra explained in [10] we can calculate the sequences of coefficients π_{2j+1} and ω_{2j+1} for both fluids. The dimensionless coordinates χ for the transmitted and reflected shock are, respectively, $\chi_t = -\tanh^{-1}\beta_t \cong -0.326419$ and $\chi_r = \tanh^{-1}\beta_r \cong 1.062157$. We show the values of the first few coefficients that allow us to calculate the initial derivative of the pressure perturbations behind each corrugated front:

$$\begin{aligned}\pi_1^a &= -0.1518432, \ \omega_1^a = -0.298504,\\ \pi_1^b &= -0.123747 \ , \ \omega_1^b = -0.087981. \end{aligned} \tag{D7}$$

The first time derivatives of the pressure perturbations behind each corrugated front (we recall that $r_t = \tau_a/\cosh\chi_t$ and $r_r = \tau_b/\cosh\chi_r$) are

$$\begin{aligned}\tilde{p}^{(1)}_{t1} &= \left.\frac{d\tilde{p}_t}{dr_t}\right|_{r_t=0+} = \frac{1}{2}\left(\pi_1^a\cosh\chi_t + \omega_1^a\sinh\chi_t\right) \cong -0.033885,\\ \tilde{p}^{(1)}_{r1} &= \left.\frac{d\tilde{p}_r}{dr_r}\right|_{r_r=0+} = \frac{1}{2}\left(\pi_1^b\cosh\chi_r + \omega_1^b\sinh\chi_r\right) \cong -0.156202. \end{aligned} \tag{D8}$$

The successive values of the initial derivatives can be calculated numerically in a systematic way. See the Supplemental Material [41] to look for the explicit analytical expressions of the first and third initial derivatives of $\tilde{p}_{t,r}$. Calculating higher order derivatives allows us to obtain the coefficients π_{2n+1} and ω_{2n+1}, necessary to plot the temporal evolution.

To calculate the first estimates of the quantities $F_{a,b}$ we must obtain the analytical form of the pressure amplitudes $F_{a1}(q_a)$ and $F_{b2}(q_b)$, to be used in Eqs. (33). The explicit forms of these functions are given in Eqs. (A7) and when written out explicitly inside the MATHEMATICA notebook they are exceedingly large. We only show here the final expressions of the auxiliary functions

$\phi_{m1,2,3}$, after substituting for the postshock and preshock background quantities:

$$\phi_{a1}(q_a) = \frac{0.209514\cosh(q_a + 0.326418)(0.111221\cosh q_a + \sqrt{1 + 0.0868714\sinh^2 q_a})}{\cosh q_a[1 + 0.315299\sinh(2q_a + 0.652837) + 1.061672\sinh^2(q_a + 0.326418)]},$$

$$\phi_{a2}(q_a) = -(0.111221\cosh q_a + \sqrt{1 + 0.0868714\sinh^2 q_a})\frac{4.495562}{\cosh q_a} \times\left[\frac{1 - 0.315299\sinh(2q_a + 0.652837) + 1.061672\sinh^2(q_a + 0.326418)}{1 + 0.315299\sinh(2q_a + 0.652837) + 1.061672\sinh^2(q_a + 0.326418)}\right],$$

$$\phi_{a3}(q_a) = \frac{0.500000\cosh q_a - 4.495562\sqrt{1 + 0.0868714\sinh^2 q_a}}{\cosh q_a},$$

$$\phi_{b1}(q_b) = -\frac{0.0269575\cosh(q_b + 1.062157)(8.991123\cosh q_b + \sqrt{1 + 11.511269\sinh^2 q_b})}{\cosh q_b[1 + 0.786488\sinh(2q_b + 2.124313) + 1.592668\sinh^2(q_b + 1.062157)]},$$

$$\phi_{b2}(q_b) = -(8.991123\sinh q_b + \sqrt{1 + 11.511269\sinh^2 q_b})\frac{0.0556104}{\cosh q_b} \times\left[\frac{1 - 0.786488\sinh(2q_b + 2.124313) + 1.592668\sinh^2(q_b + 1.062157)}{1 + 0.786488\sinh(2q_b + 2.124313) + 1.592668\sinh^2(q_b + 1.062157)}\right],$$

$$\phi_{b3}(q_b) = \frac{0.500000\cosh q_b - 0.055610\sqrt{1 + 11.511269\sinh^2 q_b}}{\cosh q_b}. \tag{D9}$$

With the auxiliary functions above we can construct the seed functions $F_{a1}^{[0]}$ and $F_{b2}^{[0]}$ with which we calculate the initial estimates of the average values $F_{a,b}$. Of course, iterating several times over Eqs. (A5), we get improved values of the bulk vorticity parameters. We obtain, as a first estimation,

$$F_{a1}^{[0]}(-2\chi_t) \cong -0.0516249, \quad F_{b2}^{[0]}(2\chi_r) \cong -0.000622197, \tag{D10}$$

and

$$F_a^{[0]} \cong -0.0798572, \;\; F_b^{[0]} \cong 0.0120960. \tag{D11}$$

If we iterate five times, we get

$$F_a^{[5]} \cong -0.0865496, \;\; F_b^{[5]} \cong 0.012538. \tag{D12}$$

With the above values, we can calculate the dimensionless asymptotic velocities at the contact surface. At first, the irrotational part is

$$u_{\text{irrot}} = \frac{\tilde{v}_{yb}^0 - R\tilde{v}_{ya}^0}{R + 1} \cong 0.224400, \tag{D13}$$

and the values for $u_i^{[0]}$ and $u_i^{[5]}$ are

$$u_i^{[0]} \cong 0.151325, \;\; u_i^{[5]} \cong 0.145287. \tag{D14}$$

For the dimensionless velocities, we get $\delta v_i^\infty \cong 5.70$ cm/ms without iterations, and $\delta v_i^\infty \cong 5.47$ cm/ms after iterating five times.

The asymptotic tangential velocities are, on the heavier fluid side,

$$v_{ia}^{[0]} \cong -0.231182, \;\; v_{ia}^{[5]} \cong -0.231836, \tag{D15}$$

which correspond to dimensional values -8.70 cm/s and -8.73 cm/s, respectively. On the side of the lighter fluid, we get

$$v_{ib}^{[0]} \cong 0.139229, \;\; v_{ib}^{[5]} \cong 0.133033, \tag{D16}$$

which correspond to dimensional values 5.24 cm/s and 5 cm/s, respectively.

We finally show the value obtained for the asymptotic ordinate ψ_∞, according to Eq. (38). For the shocked initial ripple amplitude we have $\psi_0^* \cong 0.53$ cm. The asymptotic ripple ordinate is, after using the results of Appendix A, $\psi_\infty \sim -0.4$ cm. This makes $\psi_\infty - \psi_0^* \sim -0.93$ cm, as can be seen in Fig. 19.

[1] L. D. Landau and E. M. Lifshitz, *Fluid Mechanics*, 2nd ed. (Butterworth-Heinemann, Oxford, 2000).
[2] P. M. Zaidel, J. Appl. Math. Mech. **24**, 316 (1960).
[3] M. G. Briscoe and A. A. Kovitz, J. Fluid Mech. **31**, 529 (1968).
[4] H. S. Ribner, J. Fluid Mech. **35**, 299 (1969).
[5] R. D. Richtmyer, Commun. Pure Appl. Math. **13**, 297 (1960).
[6] E. E. Meshkov, Fluid Dyn. **4**, 101 (1969).
[7] G. Fraley, Phys. Fluids **29**, 376 (1986).
[8] Y. Yang, Q. Zhang, and D. H. Sharp, Phys. Fluids **6**, 1856 (1994).
[9] A. L. Velikovich, Phys. Fluids **8**, 1666 (1996).
[10] J. G. Wouchuk and K. Nishihara, Phys. Plasmas **3**, 3761 (1996).
[11] J. G. Wouchuk and K. Nishihara, Phys. Plasmas **4**, 1028 (1997).
[12] D. Palmer Smitherman, Robert E. Chrien, Nelson M. Hoffman, and Glenn R. Magelssen, Phys. Plasmas **6**, 932 (1999).
[13] M. Brouillette and R. Bonazza, Phys. Fluids **11**, 1127 (1999).
[14] A. L. Velikovich, J. P. Dahlburg, A. J. Schmitt, J. H. Gardner, L. P. Phillips, F. L. Cochran, Y. K. Chong, G. Dimonte, and N. Metzler, Phys. Plasmas **7**, 1662 (2000).
[15] J. G. Wouchuk, Phys. Rev. E **63**, 056303 (2001).
[16] J. G. Wouchuk, Phys. Plasmas **8**, 2890 (2001).
[17] J. G. Wouchuk and K. Nishihara, Phys. Rev. E **70**, 026305 (2004).
[18] J. W. Jacobs and V. V. Krivets, Phys. Fluids **17**, 034105 (2005).
[19] A. R. Piriz, J. J. Lopez Cela, N. A. Tahir, and D. H. H. Hoffmann, Phys. Rev. E **74**, 037301 (2006).
[20] V. N. Goncharov, O. V. Gotchev, E. Vianello, T. R. Boehly, J. P. Knauer, P. W. McKenty, P. B. Radha, S. P. Regan, T. C. Sangster, S. Skupsky, V. A. Smalyuk, and R. Betti, Phys. Plasmas **13**, 012702 (2006).
[21] A. L. Velikovich, J. G. Wouchuk, C. Huete Ruiz de Lira, N. Metzler, S. Zalesak, and A. J. Schmitt, Phys. Plasmas **14**, 072706 (2007).
[22] A. R. Piriz, J. J. Lopez Cela, N. A. Tahir, and D. H. H. Hoffmann, Phys. Rev. E **78**, 056401 (2008).
[23] S. I. Abarzhi, Phys. Scr., T **132**, 014012 (2008).
[24] M. Herrmann, P. Moin, and S. I. Abarzhi, J. Fluid Mech. **612**, 311 (2008).
[25] M. Stanic, R. F. Stellingwerf, J. T. Cassibry, and S. I. Abarzhi, Phys. Plasmas **19**, 082706 (2012).
[26] M. Stanic, J. McFarland, R. F. Stellingwerf, J. T. Cassibry, D. Ranjan, R. Bonazza, J. A. Greenough, and S. I. Abarzhi, Phys. Fluids **25**, 106107 (2013).
[27] Z. Dell, R. F. Stellingwerf, and S. I. Abarzhi, Phys. Plasmas **22**, 092711 (2015).
[28] C. C. Long, V. V. Krivets, J. A. Greenough, and J. W. Jacobs, Phys. Fluids **21**, 114104 (2009).
[29] J. G. Wouchuk, C. Huete Ruiz de Lira, and A. L. Velikovich, Phys. Rev. E **79**, 066315 (2009).
[30] G. Dimonte, G. Terrones, F. J. Cherne, T. C. Germann, V. Dupont, K. Kadau, W. T. Buttler, D. M. Oro, C. Morris, and D. L. Preston, Phys. Rev. Lett. **107**, 264502 (2011).
[31] F. F. Grinstein, A. A. Gowardhan, and A. J. Wachtor, Phys. Fluids **23**, 034106 (2011).
[32] C. Huete Ruiz de Lira, A. L. Velikovich, and J. G. Wouchuk, Phys. Rev. E **83**, 056320 (2011).
[33] C. Huete, J. G. Wouchuk, and A. L. Velikovich, Phys. Rev. E **85**, 026312 (2012).
[34] C. Huete, J. G. Wouchuk, B. Canaud, and A. L. Velikovich, J. Fluid Mech. **700**, 214 (2012).
[35] A. L. Velikovich, M. Herrmann, and S. I. Abarzhi, J. Fluid Mech. **751**, 432 (2014).
[36] B. Motl, J. Oakley, D. Ranjan, C. Weber, M. Anderson, and R. Bonazza, Phys. Fluids **21**, 126102 (2009).
[37] Marc Vandemboomgaerde, Denis Souffland, Christian Mariani, Laurent Biamino, Georges Jourdan, and Lazhar Houas, Phys. Fluids **26**, 024109 (2014).
[38] D. H. Munro, Phys. Fluids B **1**, 134 (1989).
[39] F. Cobos Campos and J. G. Wouchuk, Phys. Rev. E **90**, 053007 (2014).
[40] G. B Whitham, *Linear and Nonlinear Waves* (Wiley, New York, 1974), p. 174.
[41] See Supplemental Material at http://link.aps.org/supplemental/10.1103/PhysRevE.93.053111 for more information.
[42] K. O. Mikaelian, Phys. Rev. Lett. **71**, 2903 (1993).
[43] K. O. Mikaelian, Phys. Fluids **6**, 356 (1994).
[44] J. G. Wouchuk and T. Sano, Phys. Rev. E **91**, 023005 (2015).
[45] K. O. Mikaelian, Phys. Rev. A **31**, 410 (1985).
[46] Computer code MATHEMATICA, version 10, Wolfram Research, Inc., Champaign, IL, 2014.
[47] J. Griffond, Phys. Fluids **18**, 054106 (2006).